JM PAPERS

Tailbeat perturbations improve swimming efficiency in self-propelled flapping foils

Li-Ming Chao[1,2,3], **Laibing Jia**[4] **and Liang Li**[1,2,3,†]

[1]Department of Collective Behaviour, Max Planck Institute of Animal Behavior, Konstanz 78464, Germany

[2]Centre for the Advanced Study of Collective Behaviour, University of Konstanz, Konstanz 78464, Germany

[3]Department of Biology, University of Konstanz, Konstanz 78464, Germany

[4]Department of Naval Architecture, Ocean and Marine Engineering, University of Strathclyde, Glasgow G4 0LZ, UK

Recent studies have shown that superimposing rhythmic perturbations to oscillating tailbeats could simultaneously enhance both the thrust and efficiency (Lehn *et al.*, *Phys. Rev. Fluids*, vol. 2, 2017, p. 023101; Chao *et al.*, *PNAS Nexus*, vol. 3, 2024, p. 073). However, these investigations were conducted with a tethered flapping foil, overlooking the self-propulsion intrinsic to real swimming fish. Here, we investigate how the high-frequency, low-amplitude superimposed rhythmic perturbations impact the self-propelled pitching and heaving swimming of a rigid foil. The swimming-speed-based Reynolds number ranges from 1400 to 2700 in our study, depending on superimposed perturbations and swimming modes. Numerical results reveal that perturbations significantly increase swimming speeds in both pitching and heaving motions, while enhancing efficiency exclusively in the heaving motion. Further derived scaling laws elucidate the relationships of perturbations with speeds, power costs and efficiency, respectively. These findings not only hypothesise the potential advantages of perturbations in biological systems, but also inspire designs and controls in biomimetic propulsion and manoeuvring within aquatic environments.

Key words: swimming/flying

† Email address for correspondence: lli@ab.mpg.de

1. Introduction

Nature has developed various strategies to enhance swimming efficiency while preserving swimming agility. For instance, there has been longstanding hypothesis and research regarding how fish adapt their body kinematics to achieve high swimming efficiency (Taylor, Nudds & Thomas 2003; Gazzola, Argentina & Mahadevan 2014). In addition to optimising kinematic properties like the Strouhal number (defined as the ratio of the product of vortex shedding frequency and width of the wake to the swimming velocity) (Triantafyllou, Triantafyllou & Yue 2000), recent research has unveiled that rhythmic perturbations, often considered as 'noise' and neglected, can indeed have a positive influence on the hydrodynamic performance of the tethered flapping swimmer (Lehn *et al.* 2017; Gao, Huang & Pan 2021). Lehn *et al.* (2017)'s study revealed that introducing high-frequency, low-amplitude rhythmic perturbations to a basic sinusoidal oscillation significantly improves thrust and efficiency compared with using a pure basic sinusoidal oscillation. A later study by Gao *et al.* (2021) using computational fluid dynamics (CFD) simulations with a rigid foil flapping in a flow confirmed the increase of thrust with superimposed rhythmic perturbations, but not of efficiency. This poses a question about the factors influencing efficiency since Quinn, Lauder & Smits (2014) show that the specific stiffness of a foil itself can significantly improve it. As a result, it remains uncertain whether the efficiency improvement observed by Lehn *et al.* (2017) comes from the flexibility effect, the perturbations effect, or the combination of flexibility and perturbations effects. To resolve this uncertainty, a further study by Chao *et al.* (2024) systematically investigated the impact of rhythmic perturbations on both thrust and efficiency through experiments on robotic fish, CFD simulations, and modelling. They identified the critical frequency and amplitude of perturbations, and highlighted the crucial role played by the necessary phase lag between the body motion and resulting fluid dynamics response in improving efficiency.

However, all the aforementioned studies (Lehn *et al.* 2017; Gao *et al.* 2021; Chao *et al.* 2024) were conducted on the tethered flapping foil. While in nature, fish are self-propelled by balancing the propulsive force with drag from water. This results in a positive time-averaged swimming speed and net time-averaged thrust of zero (Carling, Williams & Bowtell 1998). Recently, several investigations have been carried out in the field of self-propulsion, aimed at exploring the impact of various parameters, such as swimming kinematics (Lauder *et al.* 2007), Reynolds number (Zhang *et al.* 2018), foil thickness (Zhang *et al.* 2018), foil geometry (Zhang *et al.* 2009) and foil flexibility (Zhu, He & Zhang 2014), on the hydrodynamics of self-propelled bodies (Wang, He & Zhang 2016).

Superimposed rhythmic perturbations of high frequency and low amplitude have shown their capability to enhance both propulsive thrust and efficiency in tethered flapping motion. It is still unclear whether and, if so, how such rhythmic perturbations affect swimming performance during self-propulsion. To address this question, we conducted a comprehensive analysis of the hydrodynamic characteristics of self-propelled pitching and heaving foil using numerical and theoretical methods. The paper is structured as follows: §2 provides an introduction to the definition of superimposed rhythmic perturbations and outlines the numerical method employed; §3 presents the numerical results; §4 gives the mathematical model for predicting the swimming performance; §5 shows the wake structures generated by the self-propelled foil; and §6 summarises the findings of our study and provides a conclusion.
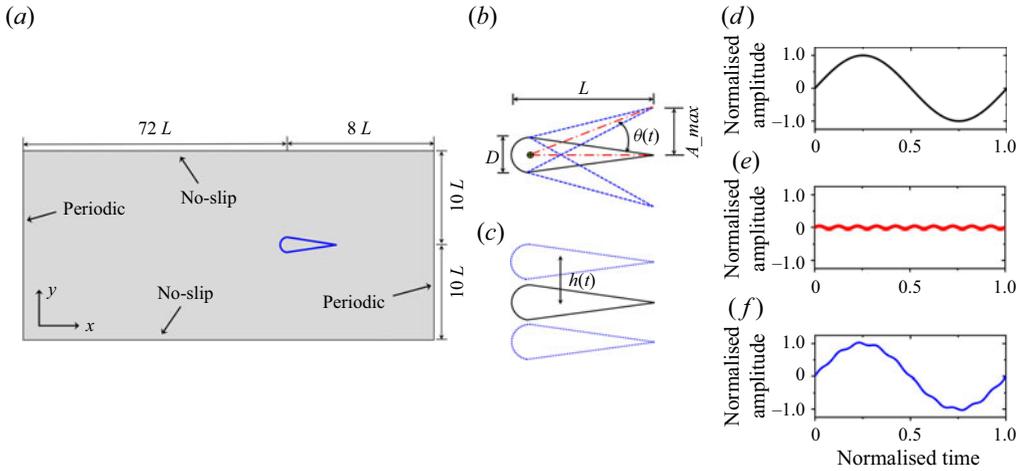
Figure 1. (*a*) Sketch of the computational domain; geometry and kinematics of the (*b*) pitching foil and (*c*) heaving foil; definition of (*d*) basic motion (BM), (*e*) perturbation motion (PM) and (*f*) accumulated motion (AM). Here, $A_{\_max}$ denotes the maximal tailbeat amplitude.

2. Problem description and methodology

A two-dimensional tear-shaped rigid foil with a semicircular leading edge of diameter D and chord length L ($D/L = 0.2$) is positioned in a quiescent fluid. The foil is free to move horizontally from right to left, and the foil's swimming direction is the negative x-axis (figure 1*a*). In the self-propelled pitching mode, the foil rotates around the centre of its semicircular leading edge, exhibiting a time-dependent pitching angle $\theta(t)$ that varies during the oscillation (figure 1*b*). In the self-propelled heaving mode, the foil oscillates transversely to the swimming direction (*y*), where its vertical movement (*y*-direction) is controlled by $h(t)$ (figure 1*c*).

We have established three modes: the basic mode (BM) characterised by a sinusoidal wave (figure 1*d*); the perturbation mode (PM) composed of high-frequency, low-amplitude oscillations (figure 1*e*); and the accumulated mode (AM), which combines the sinusoidal wave (BM) with perturbations (PM) to describe the rhythmic tailbeats of the foil (figure 1*f*). The definitions of these modes are as follows:

$$\left.\begin{aligned} A_b(t) &= A_{b\_max}\sin(2\pi f_b t) && \text{basic mode, BM,} \\ A_p(t) &= A_{p\_max}\sin(2\pi f_p t) && \text{perturbation mode, PM,} \\ A_a(t) &= A_b(t) + A_p(t) && \text{accumulated mode, AM,} \end{aligned}\right\} \quad (2.1)$$

where $A_b(t)$ and $A_p(t)$ denote the time-dependent taibeat amplitude in BM and PM, A_{b_max} and A_{p_max} describe the maximal taibeat amplitude in BM and PM, f_b and f_p refer to the oscillating frequency in BM and PM, respectively, and t is the time. In the rest of the paper, subscripts b and a refer to BM and AM, respectively. We describe the foil's motions as follows:

$$\left.\begin{aligned} A_b(t) &= \theta_b(t) = \theta_{b\_max}\sin(2\pi f_b t) && \text{BM, Pitching mode,} \\ A_p(t) &= \theta_p(t) = \theta_{p\_max}\sin(2\pi f_p t) && \text{PM, Pitching mode,} \\ A_b(t) &= h_b(t) = h_{b\_max}\sin(2\pi f_b t) && \text{BM, Heaving mode,} \\ A_p(t) &= h_p(t) = h_{p\_max}\sin(2\pi f_p t) && \text{PM, Heaving mode,} \end{aligned}\right\} \quad (2.2)$$

984 A46-3

where θ_{b_max} and θ_{p_max} refer to the maximal pitching angle in BM and PM, respectively. Since the foil thickness is $D/L = 0.2$, we have $\sin(\theta_{b\_max}) = A_{b\_max}/(L - D/2) = A_{b\_max}/0.9L$ and $\sin(\theta_{p\_max}) = A_{p\_max}/(L - D/2) = A_{p\_max}/0.9L$ for the pitching mode, respectively. However, $h_{b\_max} = A_{b\_max}$ and $h_{p\_max} = A_{p\_max}$ are the maximal heaving distance for the heaving mode in BM and PM, respectively. Without loss of generality, both the self-propelled pitching and heaving modes employ $A_{b\_max} = 0.15L$ and $f_b = 1$ Hz in our simulations.

We have introduced non-dimensionalised flapping frequency and amplitude, denoted as

$$\tilde{f} = f_p/f_b, \quad \tilde{A} = A_{p\_max}/A_{b\_max}, \tag{2.3a,b}$$

to control the superimposed perturbations. In the present study, we considered $\tilde{f} = 4 - 10$ with an interval of $\Delta\tilde{f} = 1$ and $\tilde{A} = 0.01, 0.02, 0.04, 0.05, 0.06, 0.08$ and 0.10. We further defined the swimming number (Gazzola *et al.* 2014) ratio as

$$\widetilde{Sw} = \frac{Sw_p}{Sw_b} = \frac{(2\pi L f_p A_{p\_max})/\nu}{(2\pi L f_b A_{b\_max})/\nu} = \tilde{f}\tilde{A}, \tag{2.4}$$

where ν is the fluid kinematic viscosity. To describe the swimming efficiency of the self-propelled foil, we employed the energy consumption coefficient C_E, defined as $C_E = CoT/\rho\nu^2$, where $CoT = \bar{P}/\bar{u}$ is the mechanical cost of transport (Bale *et al.* 2014; Zhang, Zhang & Huang 2022), given by the ratio of time-averaged total power ($\bar{P}$) to time-averaged steady swimming speed ($\bar{u}$), and ρ is the fluid (foil) density.

All swimming speeds observed in our simulations are normalised by the foil length L. The non-dimensionalised time-averaged swimming speed is defined as

$$\tilde{u} = \bar{u}_a/\bar{u}_b, \tag{2.5}$$

to evaluate the effect of perturbations on the swimming speed generated by self-propelled foils. Furthermore, we defined

$$\tilde{P} = \bar{P}_a/\bar{P}_b, \quad \tilde{C}_E = C_{E\_a}/C_{E\_b}, \tag{2.6a,b}$$

to assess whether AM incurs greater energy cost and enhances swimming efficiency, respectively. In (2.5) and (2.6), $\bar{u}_a$ ($\bar{u}_b$), $\bar{P}_a$ ($\bar{P}_b$) and C_{E_a} (C_{E_b}) denote the time-averaged swimming speed, time-averaged power cost and swimming efficiency generated by the self-propelled flapping foil undergoing the AM (BM) when the swimming is steady, respectively. A larger $\tilde{u}$ and $\tilde{P}$ indicate AM enjoys a faster swimming speed and greater energy consumption than BM, respectively. For AM, $\tilde{C}_E < 1$ and $\tilde{C}_E > 1$ correspond to improvements and decreases in swimming efficiency compared with the non-perturbed conditions (BM), respectively.

The unsteady flow around the self-propelled foil was simulated using the immersed boundary (IB) method (Peskin 2002). The IB method (also referred to as 'Cartesian grid methods') employs a non-body conformal Cartesian grid, where the Cartesian grids are generated regardless of the body surface. As a result, the body surface cuts through this Cartesian grid. Because the grid does not conform to the body surface, imposing the boundary conditions will require modifying the governing equations in the vicinity of the solid boundary. With the precise modifications, the governing equations can be discretized without resorting to coordinate transformation or complex discretization operators. More details about the IB method and relevant mathematical formulation can be found from Mittal & Iaccarino (2005) and Griffith & Patankar (2020). We employed the open-source CFD software IBAMR to conduct the numerical investigations (IBAMR 2014).
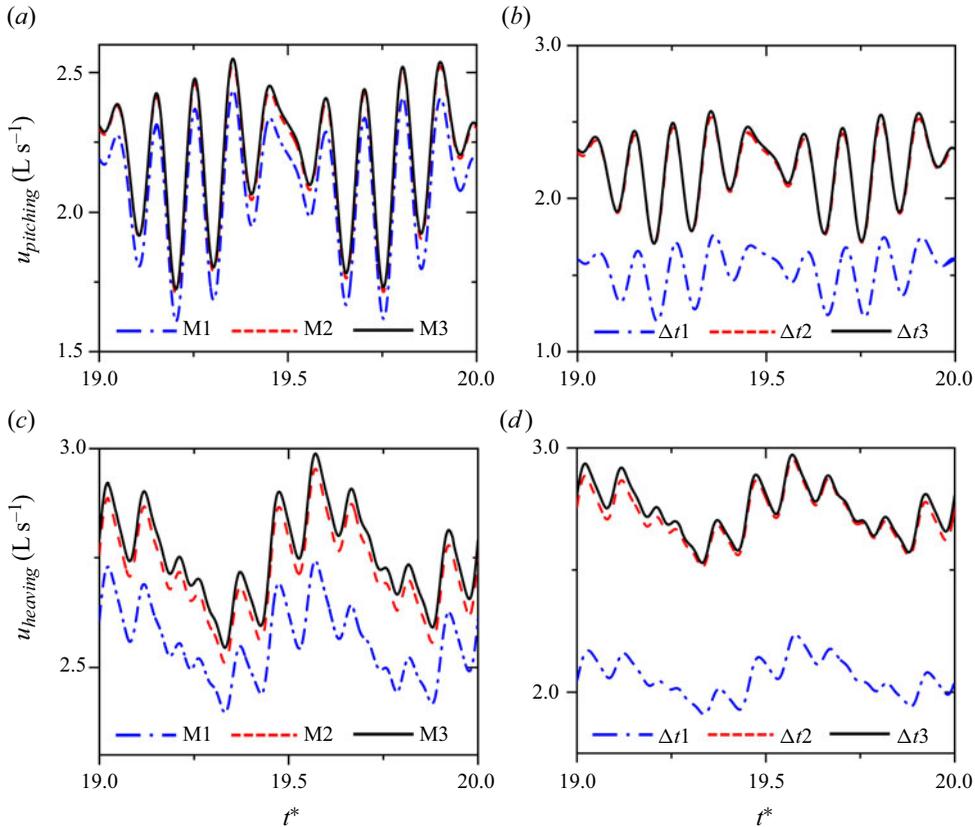
Figure 2. (*a*) Grid and (*b*) time step size convergence study of self-propelled pitching motion; (*c*) grid and (*d*) time step size convergence study of self-propelled heaving motion, respectively. $t^* = tf_b$. M1, $\Delta x/L = \Delta y/L = 0.008$; M2, $\Delta x/L = \Delta y/L = 0.005$; M3, $\Delta x/L = \Delta y/L = 0.002$. $\Delta t1$, $\Delta t \times f_p = 0.01$; $\Delta t2$, $\Delta t \times f_p = 0.001$; $\Delta t3$, $\Delta t \times f_p = 0.0005$.

This software has been widely employed to gain insights into the hydrodynamics of fish-like swimming (Bhalla *et al.* 2013*a*; Bhalla, Griffith & Patankar 2013*b*; Tytell *et al.* 2016; Hoover *et al.* 2018; Zhang *et al.* 2018; Yang & Wu 2022; Chao, Bhalla & Li 2023). In our research, we adopted a computational domain in the form of a rectangular box measuring $80 \times 20L$, with periodic boundary conditions applied along the axial direction and no-slip boundary conditions imposed in the lateral direction (figure 1*a*). To ensure statistically steady swimming, all cases were simulated for twenty normalised swimming periods $t^* = tf_b$.

The grid and time step size convergence study is conducted for both the self-propelled pitching and heaving mode with the most strenuous parameter values of $(\tilde{f}, \tilde{A}) = (10, 0.10)$. For the grid convergence study, three different grids with uniform mesh spacings of $\Delta x/L = \Delta y/L = 0.008$ (M1), 0.005 (M2) and 0.002 (M3) are considered. The time step size is fixed at $\Delta t \times f_p = 0.001$. Figures 2(*a*) and 2(*c*) present the instantaneous swimming velocity $u_{pitching}$ (self-propelled pitching mode) and $u_{heaving}$ (self-propelled heaving mode) for the three grids, respectively. Table 1 lists the time-averaged steady swimming speeds derived from the self-propelled pitching ($\bar{u}_{pitching}$) and heaving ($\bar{u}_{heaving}$) mode. There is a relatively small difference between M2 and M3, i.e. $\Delta\bar{u}_{pitching} = 0.712\%$ and $\Delta\bar{u}_{heaving} = 1.270\%$. For the remainder of the simulations, mesh M2 is selected.

Grid	$\Delta x/L$	$\bar{u}_{pitching}$ (L s^{-1})	$\Delta \bar{u}_{pitching}$ (%)	$\bar{u}_{heaving}$ (L s^{-1})	$\Delta \bar{u}_{heaving}$ (%)
M1	0.008	2.089	5.225	2.557	7.211
M2	0.005	2.188	0.712	2.721	1.270
M3	0.002	2.204	—	2.756	—

Table 1. Grid convergence study with $\Delta t \times f_p = 0.001$.

Time step size	$\Delta t \times f_p$	$\bar{u}_{pitching}$ (L s^{-1})	$\Delta \bar{u}_{pitching}$ (%)	$\bar{u}_{heaving}$ (L s^{-1})	$\Delta \bar{u}_{heaving}$ (%)
$\Delta t1$	0.01	1.536	30.502	2.059	25.039
$\Delta t2$	0.001	2.188	0.970	2.721	0.945
$\Delta t3$	0.0005	2.210	—	2.747	—

Table 2. Time-step size convergence study with $\Delta x/L = \Delta y/L = 0.005$.

Using M2, the time step size convergence study is performed by selecting three values of $\Delta t \times f_p$: $\Delta t \times f_p = 0.01$ ($\Delta t1$), 0.001 ($\Delta t2$) and 0.0005 ($\Delta t3$). The difference between the time-dependent swimming speed using $\Delta t2$ and $\Delta t3$ is negligible (figure 2b,d), where $\Delta \bar{u}_{pitching}$ and $\Delta \bar{u}_{heaving}$ is less than 1.0 % (table 2). Grid M2 and time step size $\Delta t2$ are selected based on accuracy and computational resources for the remainder of the simulations. More convergence studies related to the numerical method can be found in our previous study (Chao *et al.* 2023).

3. Results

3.1. *Self-propelled pitching mode*

Figures 3(a) and 3(b) illustrate the dependence of $\tilde{u}$ and $\tilde{P}$ on the $\tilde{f}$ and $\tilde{A}$ when the foil undergoes the self-propelled pitching motion, respectively. Both $\tilde{u}$ and $\tilde{P}$ increase as $\tilde{f}$ and/or $\tilde{A}$ increase. This indicates that stronger perturbations lead to increased energy consumption and faster swimming speeds. Furthermore, all non-dimensionalised $\tilde{u}$ values are greater than one (figure 3a), suggesting that perturbations consistently enhance the swimming speed of a self-propelled pitching foil. The non-dimensionalised swimming efficiency parameter, $\tilde{C}_E$, also exhibits a positive correlation with $\tilde{f}$ and $\tilde{A}$ (figure 3c). Notably, $\tilde{C}_E > 1$ indicates lower swimming efficiency for the self-propelled pitching foil, signifying that superimposed rhythmic perturbations reduce swimming efficiency.

We conducted further investigations to examine the impact of perturbations on the instantaneous swimming speed of the self-propelled pitching foil as it approaches a time-averaged steady swimming state in four representative scenarios: BM, $(\tilde{f}, \tilde{A}) = (5, 0.05)$, $(\tilde{f}, \tilde{A}) = (5, 0.10)$ and $(\tilde{f}, \tilde{A}) = (10, 0.10)$. As shown in figure 3($d$,$e$), it becomes evident that stronger perturbations lead to more pronounced fluctuations in $u_{pitching}$. We introduced

$$\Delta u_{pitching}^* = \frac{u_{pitching\_max\_a} - u_{pitching\_min\_a}}{u_{pitching\_max\_b} - u_{pitching\_min\_b}}, \tag{3.1}$$

to quantify these fluctuations and compare the fluctuations generated by the BM and AM, where $u_{pitching\_max\_a}$ is the maximal instantaneous swimming speed generated in AM, $u_{pitching\_min\_a}$ is the minimal instantaneous swimming speed generated in AM,
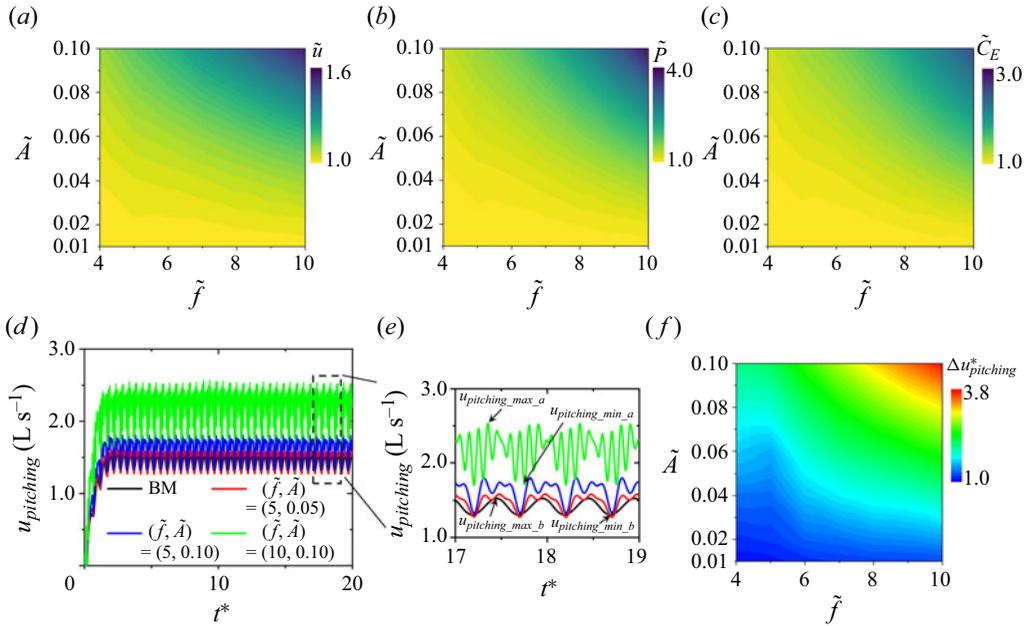
Figure 3. Dependence of (*a*) $\tilde{u}$, (*b*) $\tilde{P}$ and (*c*) $\tilde{C}_E$ on $\tilde{f}$ and $\tilde{A}$; (*d*) varying of $u_{pitching}$ at four specific cases; (*e*) zoomed-in figure of panel (*d*) at $17 \le t^* \le 19$; (*f*) non-dimensionalised fluctuations of the instantaneous swimming speed $\Delta u^*_{pitching}$ in the $\tilde{f} - \tilde{A}$ domain. Self-propelled pitching mode.

$u_{pitching\_max\_b}$ is the maximal instantaneous swimming speed generated in BM and $u_{pitching\_min\_b}$ is the minimal instantaneous swimming speed generated in BM. As figure 3(*f*) illustrates, an increase in $\tilde{f}$ and/or $\tilde{A}$ results in higher values of $\Delta u^*_{pitching}$. However, it is noted that there is no direct relationship between the $\Delta u^*_{pitching}$, represented by the non-dimensionalised fluctuations of the $u_{pitching}$, and the $\tilde{u}$, described by the non-dimensionalised mean value of the $u_{pitching}$, as both $\Delta u^*_{pitching}$ and $\tilde{u}$ positively increase with increasing $\tilde{f}$ and/or $\tilde{A}$ (figure 3*a,f*).

3.2. *Self-propelled heaving mode*

In a manner similar to the self-propelled pitching mode, the introduction of perturbations enhances the swimming speed of the self-propelled heaving foil with an increase in $\tilde{f}$ and/or $\tilde{A}$ (figure 4*a*). Comparison between figures 3(*a*) and 4(*a*) reveals that the maximal difference in $\tilde{u}$ between the self-propelled pitching and heaving modes is only 3 % ($\tilde{u} = 154\%$ and 157 % for self-propelled pitching and heaving modes, respectively). This suggests that perturbations play a similar role in affecting the steady swimming speed of the self-propelled flapping foil in both modes. Figure 4(*b*) demonstrates a positive correlation between $\tilde{P}$ and $\tilde{f}$ as well as $\tilde{A}$. Particularly, $\tilde{P} < 1.0$ when $\tilde{f}\tilde{A} < 0.47$ (as indicated by the red dashed line in the figure), implying that the foil undergoing AM with $\tilde{f}\tilde{A} < 0.47$ consumes less energy compared with the BM. As the power exchange between the heaving foil and fluid in our study is analogous to that between a cylinder undergoing prescribed or flow-induced oscillations transversely to the free stream (Han *et al.* 2023), we argue that the reduction in energy cost arises from a decrease in the phase lag ϕ between the body motion and the resulting fluid dynamics response.
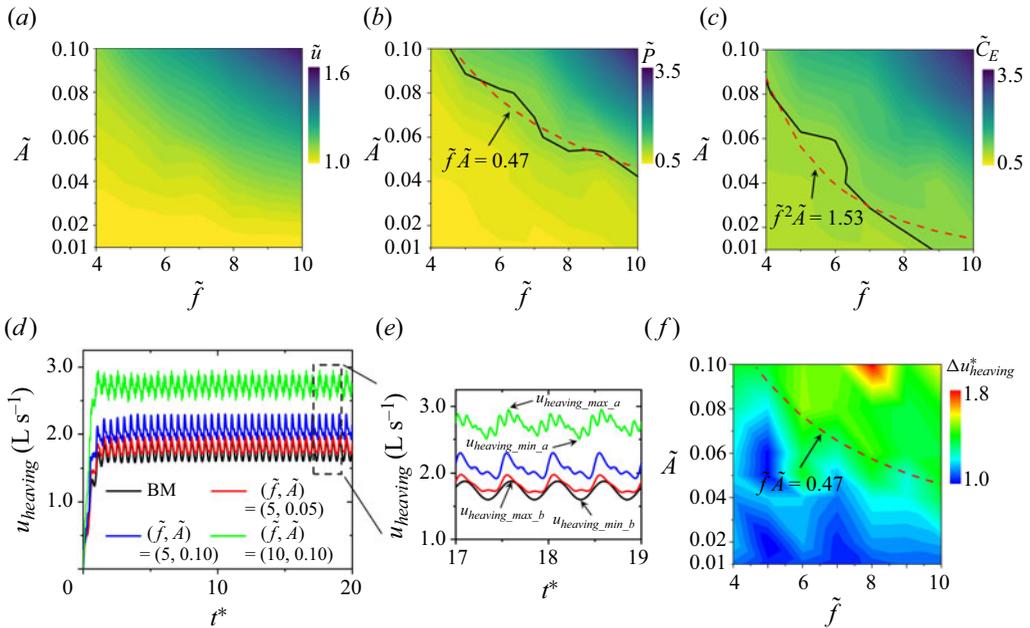
Figure 4. Dependence of (*a*) $\tilde{u}$, (*b*) $\tilde{P}$ and (*c*) $\tilde{C}_E$ on $\tilde{f}$ and $\tilde{A}$; (*d*) varying of $u_{heaving}$ at four specific cases; (*e*) zoomed-in figure of panel (*d*) at $17 \leq t^* \leq 19$; (*f*) non-dimensionalised fluctuations of the instantaneous swimming speed $\Delta u_{heaving}^*$ in the $\tilde{f} - \tilde{A}$ domain. The black solid lines in panels (*b*) and (*c*) denote $\tilde{P} = 1.0$ and $\tilde{C}_E = 1.0$, respectively. The red dashed lines in panels (*b*,*f*) and (*c*) refer to the fitting lines of $\tilde{P} = 1.0$ ($\tilde{f}\tilde{A} = 0.47$) and $\tilde{C}_E = 1.0$ ($\tilde{f}^2\tilde{A} = 1.53$), with $R^2 = 0.953$ for $\tilde{P}$ fitting and $R^2 = 0.839$ for $\tilde{C}_E$ fitting, respectively. Self-propelled heaving mode.

Further discussions are provided in the subsequent section. Given the emergence of energy savings, it is worthwhile to investigate whether the addition of perturbations improves the swimming efficiency of the self-propelled heaving foil. As illustrated in figure 4(*c*), $\tilde{C}_E < 1.0$ is observed when $\tilde{f}^2\tilde{A} < 1.53$, located at the bottom-left side of the $\tilde{f} - \tilde{A}$ map. This result demonstrates that superimposed rhythmic perturbations of high-frequency and low-amplitude can enhance both the swimming speed and efficiency of a self-propelled heaving foil, consistent with the findings in Lehn *et al.* (2017)'s study on the tethered heaving foil.

Figure 4(*d*) displays the instantaneous swimming speed $u_{heaving}$. It becomes evident that perturbations enhance both $u_{heaving\_max\_a}$ and $u_{heaving\_min\_a}$ in the self-propelled heaving mode (figure 4*e*), whereas they do not significantly affect $u_{pitching\_min\_a}$ in the self-propelled pitching mode when $\tilde{f}$ is smaller (figure 3*e*). Interestingly, figure 4(*f*) reveals that the impact of perturbations on the fluctuation of $\Delta u_{heaving}^*$ (defined similarly to $\Delta u_{pitching}^*$) is not substantial, with $\Delta u_{heaving}^* < 2.0$ in all cases. This observation suggests that the self-propelled heaving mode with perturbations results in a more stable swimming performance compared with the self-propelled pitching mode. It is also noted that the $\Delta u_{heaving}^*$ approaches to 1.0 when $\tilde{f}\tilde{A} < 0.47$, suggesting the foil would not generate a more fluctuated swimming speed compared with BM at $\tilde{P} < 1.0$ even though the perturbations have been superimposed into the base flapping motion. Furthermore, we shown more numerical results corresponding to the two-freedom self-propelled motion (foil can freely move in both *x*- and *y*-directions) in Appendix A.

984 A46-8

4. Scaling laws

4.1. *Scaling for swimming speeds*

To better understand how perturbations ($\tilde{f}$ and $\tilde{A}$) affect the non-dimensionalised swimming speed ($\tilde{u}$) of a self-propelled pitching/heaving foil, we derived scaling laws by balancing time-averaged inertial forces $\bar{F}_I = (1/nt^*) \int_\alpha^{\alpha+nt^*} F_I \, dt^*$ and viscous drag $\bar{F}_D = (1/nt^*) \int_\alpha^{\alpha+nt^*} F_D \, dt^*$ when the time-averaged swimming speed is steady, where α denotes arbitrary normalised time. For the per unit depth scales, we have $F_I \sim \rho V_{lateral}^2 L$ and $F_D \sim \mu(u/\delta)L$, where $\mu = \rho\nu$ is the fluid viscosity, $\delta \sim L/\sqrt{Re}$ is the boundary layer thickness (Gazzola *et al.* 2014), $Re = uL/\nu$ is the Reynolds number, and $V_{lateral}$ denotes the foil's lateral velocity and can be derived from the foil's kinematic equations:

$$\left.\begin{aligned}
V_{lateral} &= 2\pi f_b A_{b\_max} \cos(2\pi f_b t) \times \cos[\theta_b(t)] && \text{BM, Pitching mode,} \\
V_{lateral} &= 2\pi[f_b A_{b\_max} \cos(2\pi f_b t) + f_p A_{p\_max} \cos(2\pi f_p t)] \\
&\quad \times \cos[\theta_a(t)] && \text{AM, Pitching mode,} \\
V_{lateral} &= 2\pi f_b A_{b\_max} \cos(2\pi f_b t) && \text{BM, Heaving mode,} \\
V_{lateral} &= 2\pi[f_b A_{b\_max} \cos(2\pi f_b t) + f_p A_{p\_max} \cos(2\pi f_p t)] && \text{AM, Heaving mode.}
\end{aligned}\right\}$$

$$(4.1)$$

Considering a small θ_{b_max} and even smaller θ_{p_max} in pitching mode, we get $\cos[\theta_b(t)] \approx \cos[\theta_a(t)] \approx 1$. Equation (4.1) further suggests

$$\left.\begin{aligned}
\frac{1}{nt^*} \int_\alpha^{\alpha+nt^*} V_{lateral}^2 \, dt^* &\sim f_b^2 A_{b\_max}^2 && \text{BM,} \\
\frac{1}{nt^*} \int_\alpha^{\alpha+nt^*} V_{lateral}^2 \, dt^* &\sim f_b^2 A_{b\_max}^2 + f_p^2 A_{p\_max}^2 && \text{AM.}
\end{aligned}\right\}$$

$$(4.2)$$

By balancing $\bar{F}_I$ and $\bar{F}_D$, we obtain

$$\left.\begin{aligned}
\rho(f_b A_{b\_max})^2 L &\sim \rho\nu\bar{u}_b \left(\frac{\bar{u}_b L}{\nu}\right)^{1/2} \nu && \text{BM,} \\
\rho[(f_b A_{b\_max})^2 + (f_p A_{p\_max})^2]L &\sim \rho\nu\bar{u}_a \left(\frac{\bar{u}_a L}{\nu}\right)^{1/2} \nu && \text{AM,}
\end{aligned}\right\}$$

$$(4.3)$$

resulting in

$$\left.\begin{aligned}
\bar{u}_b &\sim (f_b A_{b\_max})^{4/3} L^{1/3} \nu^{-1/3} \sim \frac{(f_b A_{b\_max})^{4/3} L^{4/3}}{\nu^{4/3}} L^{-1} \nu && \text{BM,} \\
\bar{u}_a &\sim [(f_b A_{b\_max})^2 + (f_p A_{p\_max})^2]^{2/3} L^{1/3} \nu^{-1/3} \\
&\sim \left[\frac{(f_b A_{b\_max})^2 L^2}{\nu^2} + \frac{(f_p A_{p\_max})^2 L^2}{\nu^2}\right]^{2/3} L^{-1} \nu && \text{AM.}
\end{aligned}\right\}$$

$$(4.4)$$

Recalling $Sw_p = 2\pi L f_p A_{p\_max}/\nu$ and $Sw_b = 2\pi L f_b A_{b\_max}/\nu$ (2.4), we naturally have

$$\left.\begin{aligned}
\bar{u}_b &\sim Sw_b^{4/3} L^{-1} \nu && \text{BM,} \\
\bar{u}_a &\sim (Sw_b^2 + Sw_p^2)^{2/3} L^{-1} \nu && \text{AM.}
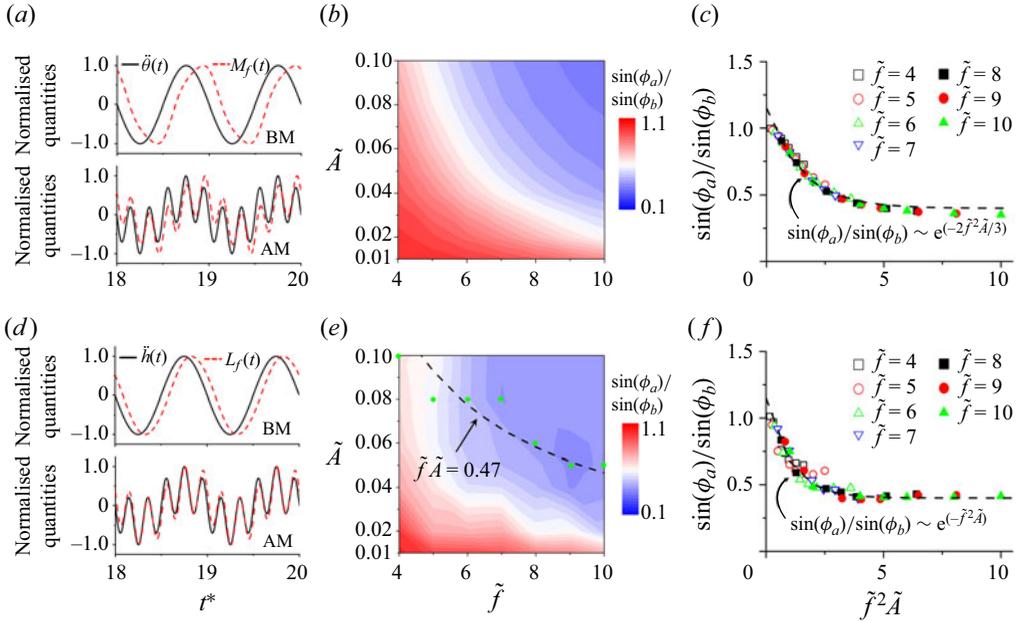\end{aligned}\right\}$$

$$(4.5)$$

Figure 5. (a) Normalised foil pitching acceleration $\ddot{\theta}(t)$ and flow-induced torque $M_f(t)$ in BM and AM, where $(\tilde{f}, \tilde{A}) = (5, 0.05)$. (b) The $\sin(\phi_a)/\sin(\phi_b)$ contour in self-propelled pitching mode. (c) Fitting for $\sin(\phi_a)/\sin(\phi_b)$ in self-propelled pitching mode, where $\sin(\phi_a)/\sin(\phi_b) \sim e^{-2\tilde{f}^2\tilde{A}/3}$. (d) Normalised foil heaving acceleration $\ddot{h}(t)$ and flow-induced lift $L_f(t)$ in BM and AM, where $(\tilde{f}, \tilde{A}) = (5, 0.05)$. (e) The $\sin(\phi_a)/\sin(\phi_b)$ contour in self-propelled heaving mode, where the dashed line refers to the $\tilde{P} = 1$ line in figure 4(b) and the green symbol denotes the location of the minimal $\sin(\phi_a)/\sin(\phi_b)$ at the specific $\tilde{f}$. (f) Fitting for $\sin(\phi_a)/\sin(\phi_b)$ in self-propelled heaving mode, where $\sin(\phi_a)/\sin(\phi_b) \sim e^{-\tilde{f}^2\tilde{A}}$.

Equation (4.5) further reveals $Re_b \sim Sw_b^{4/3}$ for BM, conforming with the works of Gazzola *et al.* (2014), while $Re_a \sim (Sw_b^2 + Sw_p^2)^{2/3}$ for AM in the viscous flow.

Based on (2.5) and (4.5), we naturally obtain

$$\tilde{u} \sim (1 + \widetilde{Sw}^2)^{2/3}, \tag{4.6}$$

where $\tilde{u}$ is always larger than 1 (4.6, figures 3a and 4a), suggesting that perturbations can constantly improve the time-averaged swimming speeds of the self-propelled foil.

4.2. *Scaling for power costs*

As mentioned in §3.2, the phase lag between the foil motion and the resulting fluid dynamics response plays an important role in affecting the power cost of a self-propelled flapping foil. Therefore, we first introduce the definitions of the phase lag in the self-propelled pitching and heaving mode before the derivation of the power cost scaling. Figure 5(a) reveals that the flow-induced torque $M_f(t)$ provided by BM remains at the same frequency with foil pitching acceleration $\ddot{\theta}(t)$, while the perturbation dominates the $M_f(t)$ profile in AM. Particularly, a phase lag ϕ exists between $M_f(t)$ and $\ddot{\theta}(t)$. Similarly, we can also observe a phase lag between flow-induced lift $L_f(t)$ and foil heaving acceleration $\ddot{h}(t)$ in the self-propelled heaving mode (figure 5d). As the state of a vibrating curve can be

modelled as a point in a Hilbert space, we use the Hilbert transform to calculate ϕ_b and ϕ_a (Williamson & Govardhan 2004) referred to as the BM-based and AM-based phase lag, respectively. Figure 5(*b,e*) reveals that $\sin(\phi_a)/\sin(\phi_b)$ decreases with an increase of $\tilde{f}$ and/or $\tilde{A}$. This tendency is attributed to the high-frequency components introduced by superimposed perturbations, which induce rapid transitions in flapping velocity and thus accelerate the response of the fluid dynamics to the flapping motion. Particularly, the minimal $\sin(\phi_a)/\sin(\phi_b)$ values at the specific $\tilde{f}$ agree well with the data-driven $\tilde{P} = 1$ line in self-propelled heaving mode (figure 5*e*), suggesting this phase lag is a critical parameter in affecting the power cost. Naturally, $\sin(\phi_a)/\sin(\phi_b)$ is a function of $\tilde{f}$ and $\tilde{A}$, and these functions corresponding to self-propelled pitching and heaving mode are fitted as

$$
\left.
\begin{aligned}
\frac{\sin(\phi_a)}{\sin(\phi_b)} &\sim e^{-2\tilde{f}^2\tilde{A}/3} \quad \text{Pitching mode,} \\
\frac{\sin(\phi_a)}{\sin(\phi_b)} &\sim e^{-\tilde{f}^2\tilde{A}} \qquad \text{Heaving mode.}
\end{aligned}
\right\}
\tag{4.7}
$$

Figure 5(*c,f*) demonstrates a good match between the numerical results and the fitted equation. However, the fitted equations also indicate that the relationship between phase difference and superimposed perturbation is highly complex.

We now go back to the power cost scaling. For the pitching foil, the time-averaged power cost is considered as the product of the net torque $M(t^*) = M_i(t^*) - M_f(t^*)$ and $\dot{\theta}(t^*)$, i.e.

$$
\bar{P} = \frac{1}{nt^*} \int_{\alpha}^{\alpha+nt^*} M(t^*)\dot{\theta}(t^*)\,\mathrm{d}t^* = \frac{1}{nt^*} \int_{\alpha}^{\alpha+nt^*} [M_i(t^*) - M_f(t^*)]\dot{\theta}(t^*)\,\mathrm{d}t^*, \tag{4.8}
$$

where inertial torque $M_i(t^*) = J\ddot{\theta}(t^*)$ with the mass moment of inertia of the foil J and flow-induced torque $M_f(t^*) = -c_1\ddot{\epsilon}(t^*) - c_2 u\dot{\epsilon}(t^*)$ with two positive coefficients $c_1 \sim L^4$ and $c_2 \sim L^3$. Here, $\ddot{\epsilon}(t^*) = \ddot{\theta}(t^* + \phi)$ and $u\dot{\epsilon}(t^*) = u\dot{\theta}(t^* + \phi)$ are sourced from the Euler angular acceleration and Coriolis acceleration of the fluid around the foil (Alam & Muhammad 2020), respectively. This phase lag ϕ, driven by diffusion-convection of the vorticity layer generated on the foil surface, corresponding to the flow retardation effect (Granger & Païdoussis 1996; Chao *et al.* 2024), is crucial in transferring power between the body and fluid (Han *et al.* 2023).

Note $\int_{\alpha}^{\alpha+nt^*} M_i(t^*)\dot{\theta}(t^*)\,\mathrm{d}t^* = \int_{\alpha}^{\alpha+nt^*} J\ddot{\theta}(t^*)\dot{\theta}(t^*)\,\mathrm{d}t^* = 0$, and the power cost is actually the integral of the product of $M_f(t^*)$ and $\dot{\theta}(t^*)$. We first calculate the flow-induced torque, as

$$
\left.
\begin{aligned}
M_b(t^*) =\ & -(4\pi^2)Jf_b^2\theta_{b\_max}\sin(2\pi f_b t^*) \\
& -(4\pi^2)c_1 f_b^2\theta_{b\_max}\sin(2\pi f_b t^* + \phi_b) \\
& +(2\pi)c_2 u_b f_b\theta_{b\_max}\cos(2\pi f_b t^* + \phi_b) \qquad\qquad\qquad \text{BM,} \\
M_a(t^*) =\ & -(4\pi^2)J[f_b^2\theta_{b\_max}\sin(2\pi f_b t^*) + f_p^2\theta_{p\_max}\sin(2\pi f_p t^*)] \\
& -(4\pi^2)c_1[f_b^2\theta_{b\_max}\sin(2\pi f_b t^* + \phi_a) + f_p^2\theta_{p\_max}\sin(2\pi f_p t^* + \phi_a)] \\
& +(2\pi)c_2 u_a[f_b\theta_{b\_max}\cos(2\pi f_b t^* + \phi_a) + f_p\theta_{p\_max}\cos(2\pi f_p t^* + \phi_a)], \quad \text{AM,}
\end{aligned}
\right\}
\tag{4.9}
$$

where ϕ_b and ϕ_a refer to the phase lag in BM and AM, respectively. The $\dot{\theta}(t)$ can be directly obtained from the kinematics, as

$$\left.\begin{array}{ll} \dot{\theta}_b(t) = 2\pi f_b \theta_{b\_max} \cos(2\pi f_b t) & \text{BM,} \\ \dot{\theta}_a(t) = 2\pi[f_b \theta_{b\_max} \cos(2\pi f_b t) + f_p \theta_{p\_max} \cos(2\pi f_p t)] & \text{AM.} \end{array}\right\} \quad (4.10)$$

Therefore, time-averaged power costs read as

$$\left.\begin{array}{l} \bar{P}_b(t) \sim -c_3 L f_b^3 \theta_{b\_max}^2 \sin(\phi_b) + \bar{u}_b f_b^2 \theta_{b\_max}^2 \cos(\phi_b) \\[2mm] \sim \left[-c_3 \dfrac{L^3 f_b^3 \theta_{b\_max}^3}{v^3} \theta_{b\_max}^{-1} v \sin(\phi_b) + \bar{u}_b \dfrac{L^2 f_b^2 \theta_{b\_max}^2}{v^2} \cos(\phi_b) \right] L^{-2} v^2 \\[3mm] \sim [-c_3 Sw_b^3 \theta_{b\_max}^{-1} v \sin(\phi_b) + \bar{u}_b Sw_b^2 \cos(\phi_b)] L^{-2} v^2 \qquad \text{BM,} \\[3mm] \bar{P}_a(t) \sim -c_3 L(f_b^3 \theta_{b\_max}^2 + f_p^3 \theta_{p\_max}^2) \sin(\phi_a) + \bar{u}_a(f_b^2 \theta_{b\_max}^2 + f_p^2 \theta_{p\_max}^2) \cos(\phi_a) \\[3mm] \sim \left[-c_3 \left(\dfrac{L^3 f_b^3 \theta_{b\_max}^3}{v^3} \theta_{b\_max}^{-1} + \dfrac{L^3 f_p^3 \theta_{p\_max}^3}{v^3} \theta_{p\_max}^{-1} \right) v \sin(\phi_a) \right] L^{-2} v^2 \\[3mm] \quad + \bar{u}_a \left[\left(\dfrac{L^2 f_b^2 \theta_{b\_max}^2}{v^2} + \dfrac{L^2 f_p^2 \theta_{p\_max}^2}{v^2} \right) \cos(\phi_a) \right] L^{-2} v^2 \\[3mm] \sim [-c_3(Sw_b^3 \theta_{b\_max}^{-1} + Sw_p^3 \theta_{p\_max}^{-1}) v \sin(\phi_a)] L^{-2} v^2 \\[2mm] \quad + \bar{u}_a[(Sw_b^2 + Sw_p^2) \cos(\phi_a)] L^{-2} v^2 \qquad \text{AM,} \end{array}\right\} \quad (4.11)$$

with the positive coefficient c_3. Then, we have the $\tilde{P}$ scaling for the pitching foil as

$$\begin{aligned} \tilde{P} &\sim \frac{-c_3(Sw_b^3 \theta_{b\_max}^{-1} + Sw_p^3 \theta_{p\_max}^{-1}) v \sin(\phi_a) + \bar{u}_a(Sw_b^2 + Sw_p^2) \cos(\phi_a)}{-c_3 Sw_b^3 \theta_{b\_max}^{-1} v \sin(\phi_b) + \bar{u}_b Sw_b^2 \cos(\phi_b)} \\[3mm] &\sim \frac{-c_3(Sw_b \theta_{b\_max}^{-1} + \widetilde{Sw}^2 Sw_p \theta_{p\_max}^{-1}) v \sin(\phi_a) + \bar{u}_a(1 + \widetilde{Sw}^2) \cos(\phi_a)}{-c_3 Sw_b \theta_{b\_max}^{-1} v \sin(\phi_b) + \bar{u}_b \cos(\phi_b)} \\[3mm] &\sim \frac{-c_3 Sw_b(\tilde{\theta} + \widetilde{Sw}^3) v \sin(\phi_a) + \theta_{p\_max} \bar{u}_a(1 + \widetilde{Sw}^2) \cos(\phi_a)}{-c_3 Sw_b \tilde{\theta} v \sin(\phi_b) + \theta_{p\_max} \bar{u}_b \cos(\phi_b)} \\[3mm] &\sim \frac{-c_3 Sw_b(\tilde{\theta} + \widetilde{Sw}^3) v \sin(\phi_a) + c_4 \theta_{p\_max} \bar{u}_b(1 + \widetilde{Sw}^2)^{5/3} \cos(\phi_a)}{-c_3 Sw_b \tilde{\theta} v \sin(\phi_b) + \theta_{p\_max} \bar{u}_b \cos(\phi_b)}, \end{aligned} \quad (4.12)$$

where c_4 is a positive coefficient. For the low-amplitude pitching, we have $\tilde{\theta} = \theta_{p\_max}/\theta_{b\_max} = A_{p\_max}/A_{b\_max} = \tilde{A}$ and $\theta_{p\_max} \approx 0$, and therefore

$$\tilde{P} \sim \frac{-c_3 Sw_b(\tilde{\theta} + \widetilde{Sw}^3) v \sin(\phi_a)}{-c_3 Sw_b \tilde{\theta} v \sin(\phi_b)} \sim (1 + \tilde{A}^{-1}\widetilde{Sw}^3) \cdot \frac{\sin(\phi_a)}{\sin(\phi_b)}. \quad (4.13)$$

Similar to the pitching motion, we have the time-averaged power cost of the heaving foil as

$$\bar{P} = \frac{1}{nt^*} \int_\alpha^{\alpha + nt^*} [L_i(t^*) - L_f(t^*)] \dot{h}(t^*) \, dt^*, \quad (4.14)$$

where $L_i(t^*)$ and $L_f(t^*)$ refer to the inertial and flow-induced lift, respectively, and $L_i(t^*) \sim \ddot{h}(t^*)$. Different from the condition in self-propelled pitching mode, we have $L_f(t^*) = -c_5 \ddot{\epsilon}(t^*)$ with a coefficient c_5. Therefore, we have

$$\tilde{P} \sim \frac{Sw_b(\tilde{h} + \widetilde{Sw}^3)\nu \sin(\phi_a)}{Sw_b\tilde{h}\nu \sin(\phi_b)} \sim (1 + \tilde{A}^{-1}\widetilde{Sw}^3) \cdot \frac{\sin(\phi_a)}{\sin(\phi_b)}, \tag{4.15}$$

where $\tilde{A} = \tilde{h} = h_{p\_max}/h_{b\_max}$.

Overall, the scaling for power costs is

$$\tilde{P} \sim (1 + \tilde{A}^{-1}\widetilde{Sw}^3) \cdot \frac{\sin(\phi_a)}{\sin(\phi_b)}. \tag{4.16}$$

Equation (4.16) suggests that the power costs increase in AM is not only dependent on the input perturbations ($\tilde{f}$ and $\tilde{A}$), but also affected by the phase lag between the foil motion and the resulting fluid dynamic response. Even with the same input perturbations, the different flapping kinematics may generate different phase lags (figure 5b,e), therefore resulting in different power costs (figures 3b,4b).

4.3. *Scaling for swimming efficiencies*

Based on (4.6) and (4.16), the non-dimensionalised swimming efficiency $\tilde{C}_E$ can be scaled as

$$\tilde{C}_E = \tilde{P} \cdot \tilde{u}^{-1} \sim \frac{1 + \tilde{A}^{-1}\widetilde{Sw}^3}{(1 + \widetilde{Sw}^2)^{2/3}} \cdot \frac{\sin(\phi_a)}{\sin(\phi_b)}. \tag{4.17}$$

Equation (4.17) suggests that the efficiency improvement sourced from adding perturbations is affected by the non-dimensionalised amplitude, non-dimensionalised swimming number and phase lag. Referring to the research conducted by Floryan, Van Buren & Smits (2018), the authors noted that the efficiency of a flapping foil is governed by both the flapping amplitude and the Strouhal number, a pattern akin to our (4.17). In particular, we demonstrated that the efficiency of a self-propelled foil can be enhanced by reducing the phase lag between the foil motion and the resulting fluid dynamics response.

To assess the compatibility of the scaling laws mentioned above with the simulated data of the self-propelled flapping foil, we created plots of $\tilde{u}$, $\tilde{P}$ and $\tilde{C}_E$ against the parameters associated with perturbations: $(1 + \widetilde{Sw}^2)^{2/3}$, $1 + \tilde{A}^{-1}Sw^3$ and $(1 + \tilde{A}^{-1}Sw^3)/(1 + \widetilde{Sw}^2)^{2/3}$. These are presented in figure 6(a–c) for the self-propelled pitching mode and in figure 6(d–f) for the self-propelled heaving mode. The numerical data align remarkably well on a single linear curve, suggesting that the current scaling laws can accurately predict the hydrodynamic performance of self-propelled foils undergoing flapping with superimposed perturbations.

5. Wake structures

Several distinguished wake structures generated by the self-propelled pitching foil are identified: reverse Kármán vortex (RKV) wake, symmetric wake (SW) I, symmetric wake (SW) II-A, symmetric wake (SW) II-B, asymmetric wake (AsW) I, asymmetric wake (AsW) II and 2P wake (Williamson & Roshko 1988). The representative flow structures and their presence in the $\tilde{f} - \tilde{A}$ domain are shown in figure 7. The classical RKV wake is
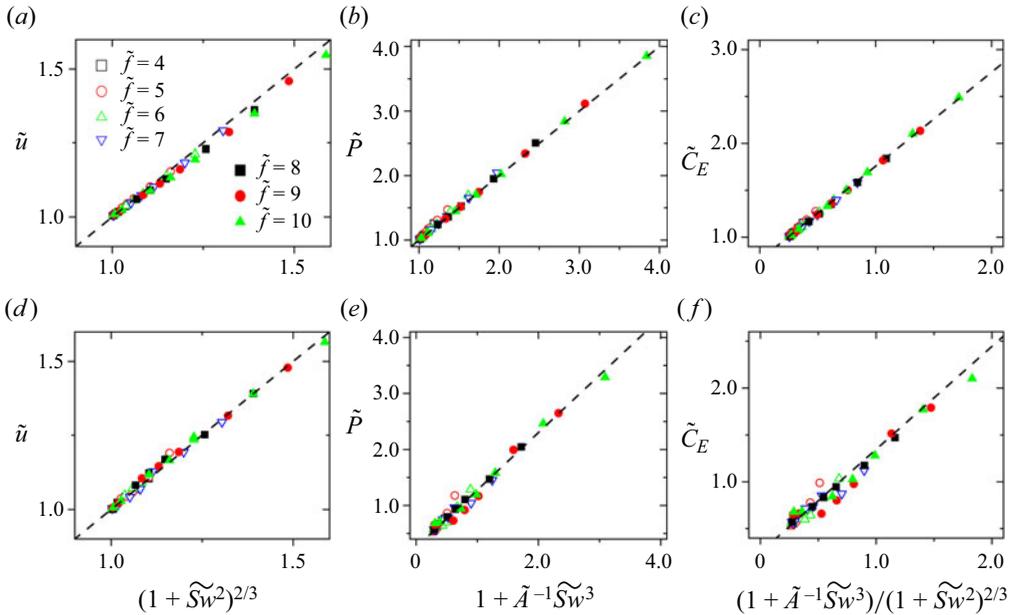
Figure 6. Scaling for the (*a*) $\tilde{u}$, (*b*) $\tilde{P}$ and (*c*) $\tilde{C}_E$ in the self-propelled pitching mode and (*d*) $\tilde{u}$, (*e*) $\tilde{P}$ and (*f*) $\tilde{C}_E$ in the self-propelled heaving mode, respectively.

observed when the pitching foil employs BM, where the vortices from a side of the foil take the opposite side of the wake (figure 7*b*). When $\tilde{f}$ is an odd number ($\tilde{f} = 5$, 7, 9), the symmetric wake, including SW I, SW II-A and SW II-B, emerges behind the foil depending on both $\tilde{f}$ and $\tilde{A}$. The SW I forming as the RKV wake is observed at $\tilde{f} = 5$ and $(\tilde{f}, \tilde{A}) = (7, 0.01)$ (figure 7*c*). The emergence of the SW I is found at $(\tilde{f}, \tilde{A}) = (7, 0.02)$ and $(\tilde{f} = 9, \tilde{A} \leq 0.05)$, where the wake involves the primary vortex (PV) and secondary vortex (SV) (figure 7*d*). The PV consists of a stronger main vortex pair occupied the position behind the foil's symmetric line, and weaker negative/positive vorticity located at the upper and bottom sides of the main vortex pair, respectively, while the SV forms the RKV wake. With a little increase in $\tilde{f}$ and /or $\tilde{A}$, the SW II-A transmutes to SW II-B (figure 7*e*), where the SV transits from the reverse Kármán vortex wake to the Kármán vortex (KV) wake. The asymmetric wake (AsW I and II) and 2P wake are observed when $\tilde{f}$ is an even number ($\tilde{f} = 4$, 6, 8, 10). The AsW I dominates the majority of the $\tilde{f} - \tilde{A}$ domain, manifesting as a downward deflection of the RKV wake (figure 7*f*). When $(\tilde{f}, \tilde{A}) = (8, 0.10)$, the vortices close to the foil's trailing edge fail to rapidly coalesce into a stronger vortex core, giving rise to the PV resembling 2P wake. Conversely, vortices farther from the foil's trailing edge evolve and experience viscous effects, forming a deflected RKV wake (figure 7*g*). The 2P wake is observed at $(\tilde{f}, \tilde{A}) = (10, 0.10)$. It is noted that the deflection of wake structure is influenced by whether $\tilde{f}$ is an odd or even number. When $\tilde{f}$ is an odd number, PM and BM are in phase, meaning that perturbations amplify the maximum flapping amplitude at $t/T_b = 0.25$. However, the flapping amplitude under AM is equal to that under BM when $\tilde{f}$ is an even number and $t/T_b = 0.25$, while the emergency of the maximum flapping amplitude is advanced (figure 8).
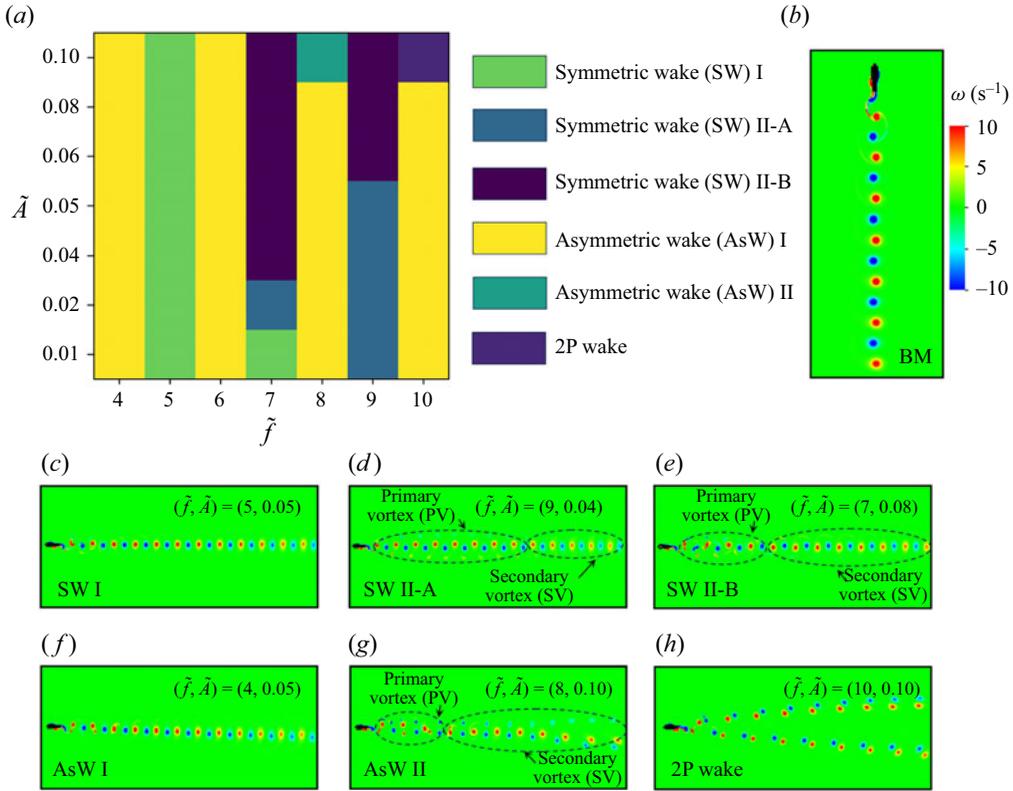
984 A46-14

Figure 7. (*a*) Wake structure map in the self-propelled pitching mode. Typical instantaneous vorticity structures: (*b*) reverse Kármán vortex (BM); (*c*) symmetric wake (SW) I ($\tilde{f} = 5$, $\tilde{A} = 0.05$); (*d*) symmetric wake (SW) II-A ($\tilde{f} = 9$, $\tilde{A} = 0.04$); (*e*) symmetric wake (SW) II-B ($\tilde{f} = 7$, $\tilde{A} = 0.08$); (*f*) asymmetric wake (AsW) I ($\tilde{f} = 4$, $\tilde{A} = 0.05$); (*g*) asymmetric wake (AsW) II ($\tilde{f} = 8$, $\tilde{A} = 0.10$); (*h*) 2P wake ($\tilde{f} = 10$, $\tilde{A} = 0.10$).
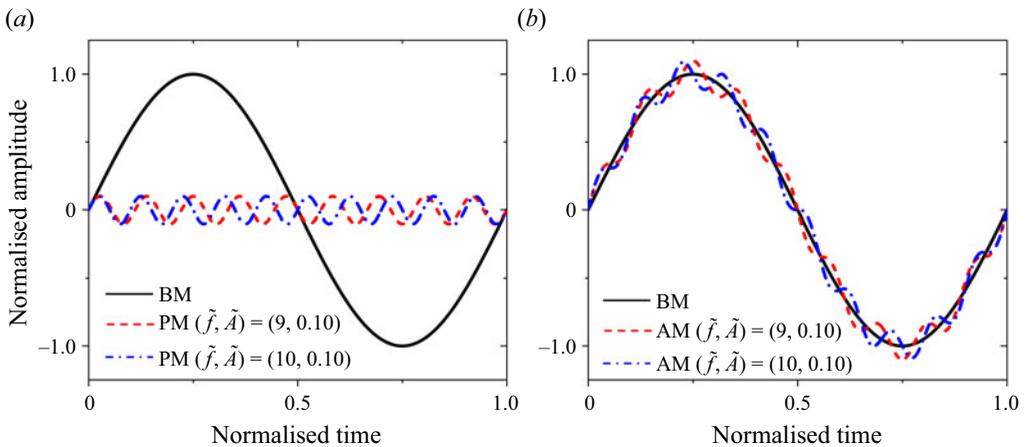
Figure 8. (*a*) Varying of foil's pitching amplitude of BM and PM; (*b*) varying of foil's pitching amplitude of BM and AM.
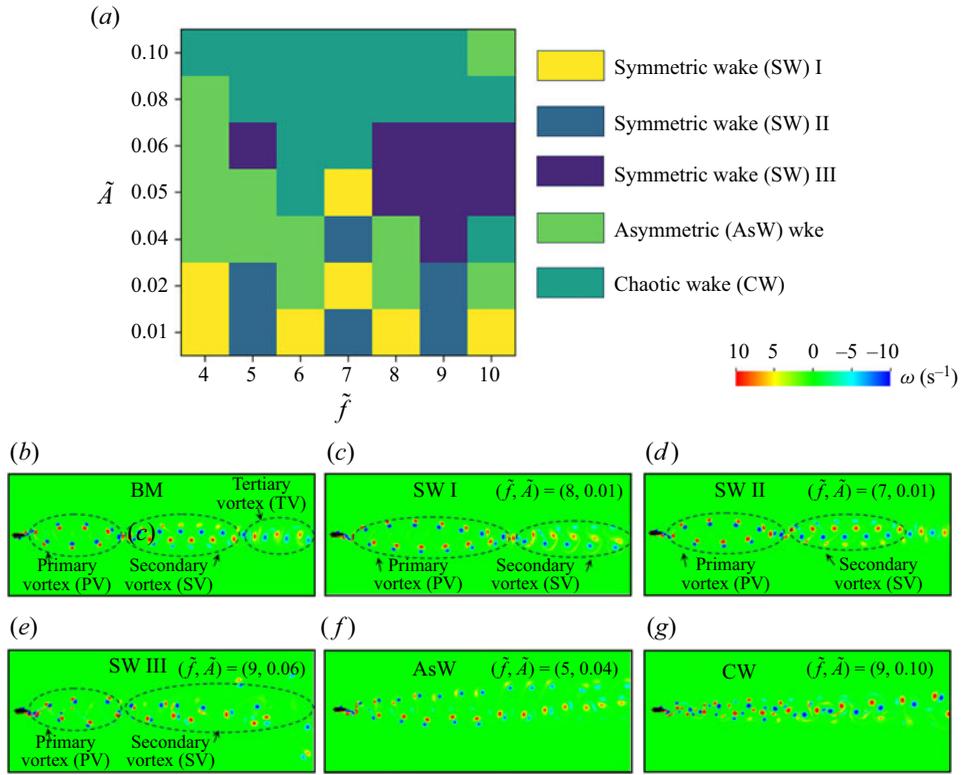
Figure 9. (*a*) Wake structure map in the self-heaving pitching mode. Typical instantaneous vorticity structures: (*b*) symmetric wake (BM); (*c*) symmetric wake (SW) I ($\tilde{f} = 8, \tilde{A} = 0.01$); (*d*) symmetric wake (SW) II ($\tilde{f} = 7$, $\tilde{A} = 0.01$); (*e*) symmetric wake (SW) III ($\tilde{f} = 9, \tilde{A} = 0.06$); (*f*) asymmetric wake (AsW) ($\tilde{f} = 5, \tilde{A} = 0.04$); (*g*) chaotic wake (CW) II ($\tilde{f} = 9, \tilde{A} = 0.10$).

Compared with the wake structures generated by the self-propelled pitching foil, the relationship between flow patterns provided by the self-propelled heaving foil and superimposed perturbations ($\tilde{f}, \tilde{A}$) is intricate (figure 9*a*). When the heaving foil undergoes the BM, it generates a symmetric wake composed of the PV, SV and tertiary vortex (TV): the PV takes shape as a 2P wake, the SV incorporates a main KV wake positioned behind the foil's symmetry line, with weaker positive/negative vorticity located on the upper and lower sides of the main KV wake, respectively, and the TV manifests as the RKV wake (figure 9*b*). As the flow patterns generated by the self-propelled heaving foil are complicated, we considered the symmetry of wake structures only from the PV. Only PV and SV are considered when the wake structures produced by the AM are identified. When the self-propelled heaving foil generates the symmetric wake (SW I, II and III), the PV constantly forms as the 2P wake, while the SV can be the deflected RKV wake (SW I, figure 9*c*), the main RKV wake positioned behind the foil's symmetry line (SW II, figure 9*d*), and the chaotic wake (SW III, figure 9*e*). The AsW describes the bifurcation flow deflected upwards or downwards (figure 9*f*). The CW (chaotic wake) is obscure, and we cannot identify meaningful mP+nS vortex structures (Williamson & Roshko 1988) from this flow field. Furthermore, The influence of the odd or even nature of $\tilde{f}$ on the flow structures is only significant when $\tilde{A} = 0.01$.

984 A46-16

In previous studies, researchers reported a smooth increase in propulsive force with an increase in flapping frequency and/or amplitude, accompanied by a smooth transition of the flow structures provided by the tethered flapping foil (KV → RKV → deflected RKV wake) (Godoy-Diana, Aider & Wesfreid 2008; Andersen *et al.* 2017; Chao, Alam & Ji 2021). However, we found that the swimming speed produced by the self-propelled pitching/heaving foil with perturbations smoothly increases with the increment of $\tilde{f}$ and $\tilde{A}$, while the transition of the wake structures is not smooth. This observation raises a question: Could swimmers' wake structures be reliable for predicting swimming performance? In the studies on the tethered flapping foil, some researchers suggested that the wake structures can be the footprints of a flapping foil and be used to predict the force generation (Zhang 2017), while others suggested that the swimmers' wake structures are not reliable indicators of swimming performance (Floryan, Van Buren & Smits 2020). Due to our results indicating that the speed generation of self-propelled flapping foil largely aligns with the predictions of linear theory (Garrick 1936), we argue that the mode of the vortex wakes behind a self-propelled flapping foil with perturbations seems to be a remnant of speed generation, rather than a driver (Mackowski & Williamson 2015). Wake structures generated by the self-propelled flapping foil are shown in Appendix B (figures 12 and 13) and supplementary movie 1 available at https://doi.org/10.1017/jfm.2024.262.

6. Conclusions

In this study, we conducted a systematic investigation into the influence of superimposed rhythmic perturbations characterised by high-frequency and low-amplitude on the performance of a self-propelled flapping foil. Our results showed a notable enhancement in time-averaged swimming speeds with the introduction of these perturbations. Stronger perturbations lead to faster swimming speeds. Particularly, we also observed that appropriate perturbation inputs can significantly improve the swimming efficiency of the self-propelled heaving foil. To explain these phenomena, we established scaling laws to elucidate how these perturbations influence swimming speed and efficiency in self-propelled bodies, focusing particularly on the importance of phase lag between the foil motion and the resulting fluid dynamics response in modulating power exchange. Overall, our results upend the standard belief that categorises high-frequency and low-amplitude perturbations as insignificant 'noise.' Our data suggest that these perturbations may actually be 'auspiciousness', positively affecting swimming performance.

The effect of low-amplitude and high-frequency flapping on the flyer's performance has also been studied in previous works (Cleaver 2011; Cleaver *et al.* 2011). For instance, Bomphrey *et al.* (2017) revealed that mosquitoes can capture the power of shedding vortex through low-amplitude and high-frequency flapping motion. For swimming organisms, the coupling between perturbations and fundamental pitching/heaving movements can be considered as the passive/active response of the organisms' muscles. On the one hand, perturbations may be regarded as passive vibrations of muscles in response to the coupling between fish motion and the surrounding flow field (Fish & Lauder 2006), essentially representing the dynamic response of organisms to their environment. On the other hand, organisms may actively generate these perturbations to alter the flow field around them, adapting to different motion requirements or environmental conditions. However, it is difficult to observe significant muscle motions sourced from perturbations. We speculate that these perturbations may exist at the microscopic level, and they may be more pronounced during the early stages of fish development since the larval fish exhibit

more random body waves while adults exhibit clearer stereotypical sinusoidal tailbeat kinematics (Muller & Van Leeuwen 2004).

Examining the effects of high-frequency, low-amplitude superimposed perturbations provides a promising path for future research (such as the flapping motion combined with both pitching and heaving motions, Appendix C). These perturbations more closely mimic the complex environmental challenges faced by organisms in their natural habitats, such as the turbulent eddies accompanying aquatic locomotion. Our findings lay the groundwork for practical applications, suggesting that careful use of these perturbations can bring substantial benefits. Specifically, we foresee potential improvements in thrust and efficiency across a wide range of underwater robotic technologies and propulsion systems.

Supplementary movie. Supplementary movie is available at https://doi.org/10.1017/jfm.2024.262.

Author ORCIDs.
- Li-Ming Chao https://orcid.org/0000-0002-8800-6065;
- Laibing Jia https://orcid.org/0000-0003-1327-5516;
- Liang Li https://orcid.org/0000-0002-2447-6295.

Appendix A. Two-freedom self-propelled motion

We have also simulated the self-propulsion of the flapping foil where the foil can freely move in both the horizontal (x) and lateral (y) directions simultaneously (two-freedom self-propelled motion). The $\tilde{f}$ ranges from 5 to 10 with an interval of 1, and $\tilde{A} = 0.02 - 0.10$ with an interval of 0.02. Figure 10(a–c) illustrates the dependence of the $\tilde{u}$, $\tilde{P}$ and $\tilde{C}_E$ on the $\tilde{f}$ and $\tilde{A}$ when the foil undergoes two-freedom self-propelled pitching motion. Similar to the results of one-freedom motion, $\tilde{u}$, $\tilde{P}$ and $\tilde{C}_E$ increase with an increase in $\tilde{f}$ and/or $\tilde{A}$, suggesting the superimposed perturbations can improve the swimming speed but cannot improve the swimming efficiency in the self-propelled pitching mode. Particularly, we found that the two-freedom motion with perturbations needs more power to generate the forward swimming since the $\tilde{P}$ in figure 10(b) is larger than that in figure 3(b) with the specific ($\tilde{f}$, $\tilde{A}$). We further considered the feasibility of our scaling laws when the foil undergoes two-freedom self-propelled motion. As shown in figures 10(d)–10(f), the $\tilde{u}$, $\tilde{P}$ and $\tilde{C}_E$ linearly relate to the $(1 + \widetilde{Sw}^2)^{2/3}$, $1 + \tilde{A}^{-1}\widetilde{Sw}^3$ and $(1 + \tilde{A}^{-1}\widetilde{Sw}^3)/(1 + \widetilde{Sw}^2)^{2/3}$, respectively, where the slope of $\tilde{P}$ and $\tilde{C}_E$ scaling lines in two-freedom self-propelled motion is larger than that in one-freedom self-propelled motion. However, we found that the fitting performance at $(\tilde{f}, \tilde{A}) = (10, 0.10)$ is unsatisfactory, suggesting that our scaling law has some limitations in describing two-freedom self-propelled motion with greater superimposed perturbations.

However, the self-propelled heaving foil cannot generate effective swimming speed when it moves freely in both x- and y-directions. As shown in figure 11, both BM and AM provide the time-mean horizontal and lateral swimming speeds approaching zero
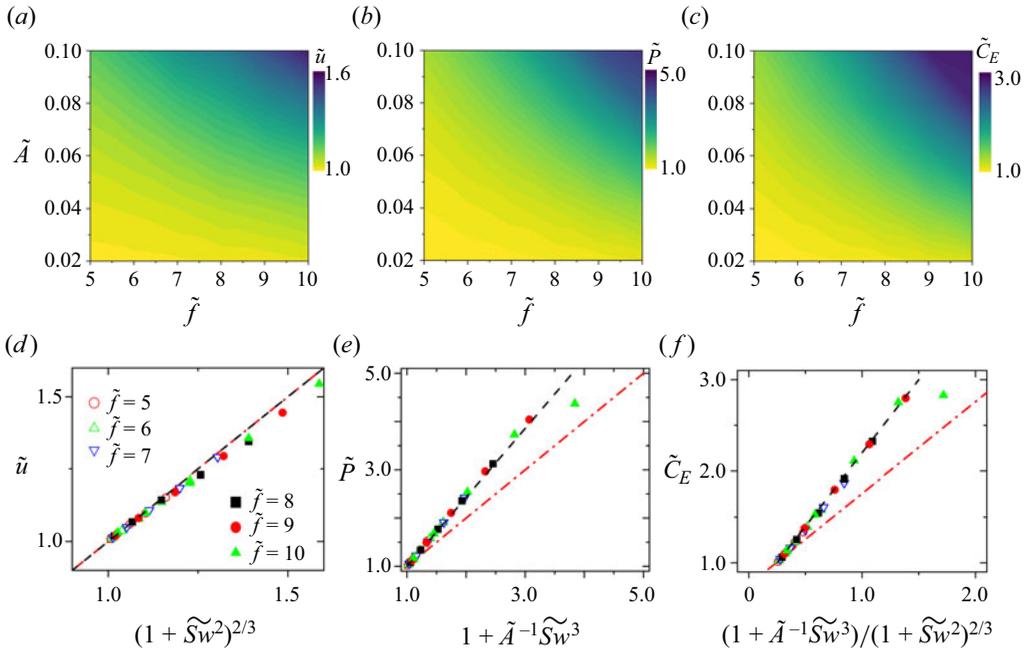
Figure 10. Dependence of (*a*) $\tilde{u}$, (*b*) $\tilde{P}$ and (*c*) $\tilde{C}_E$ on $\tilde{f}$ and $\tilde{A}$; scaling for (*d*) $\tilde{u}$, (*e*) $\tilde{P}$ and (*f*) $\tilde{C}_E$. Foil freely propels itself in both the *x*- and *y*-directions. The dashed black and dash-dotted red lines in panels (*d*)–(*f*) refer to the fitting lines for two-freedom and one-freedom self-propelled pitching motion, respectively.
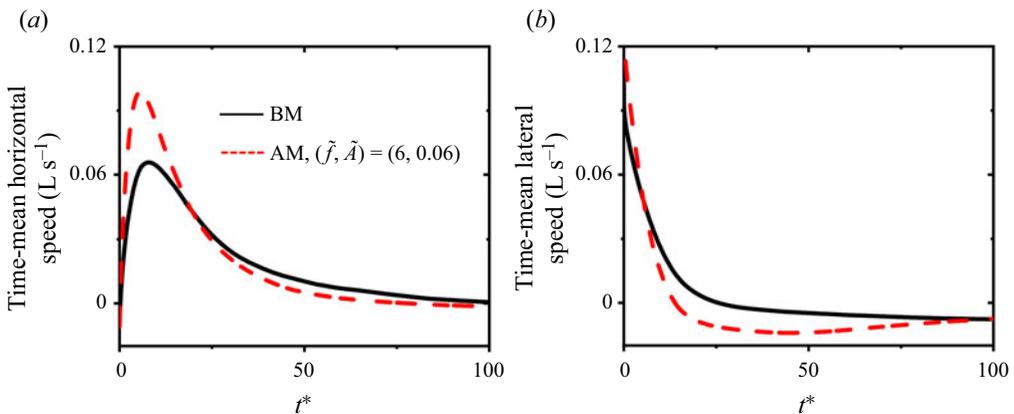

Figure 11. (*a*) Time-mean horizontal speed; (*b*) time-mean lateral speed. Two-freedom self-propelled heaving motion.

after long-term simulations ($t^* = t/T_b = 100$). Considering that the self-propulsion arises from the balance between the inertia and viscous forces, we argue the present symmetric heaving motion with a smaller amplitude and zero angle of attack cannot generate effective thrust. Furthermore, we also noted that the previous works on the self-propelled heaving body were mainly conducted on the one-freedom motion (Zhang *et al.* 2009; Becker *et al.* 2015; Marquet *et al.* 2021).

Appendix B. Wake structures generated by the self-propelled foil
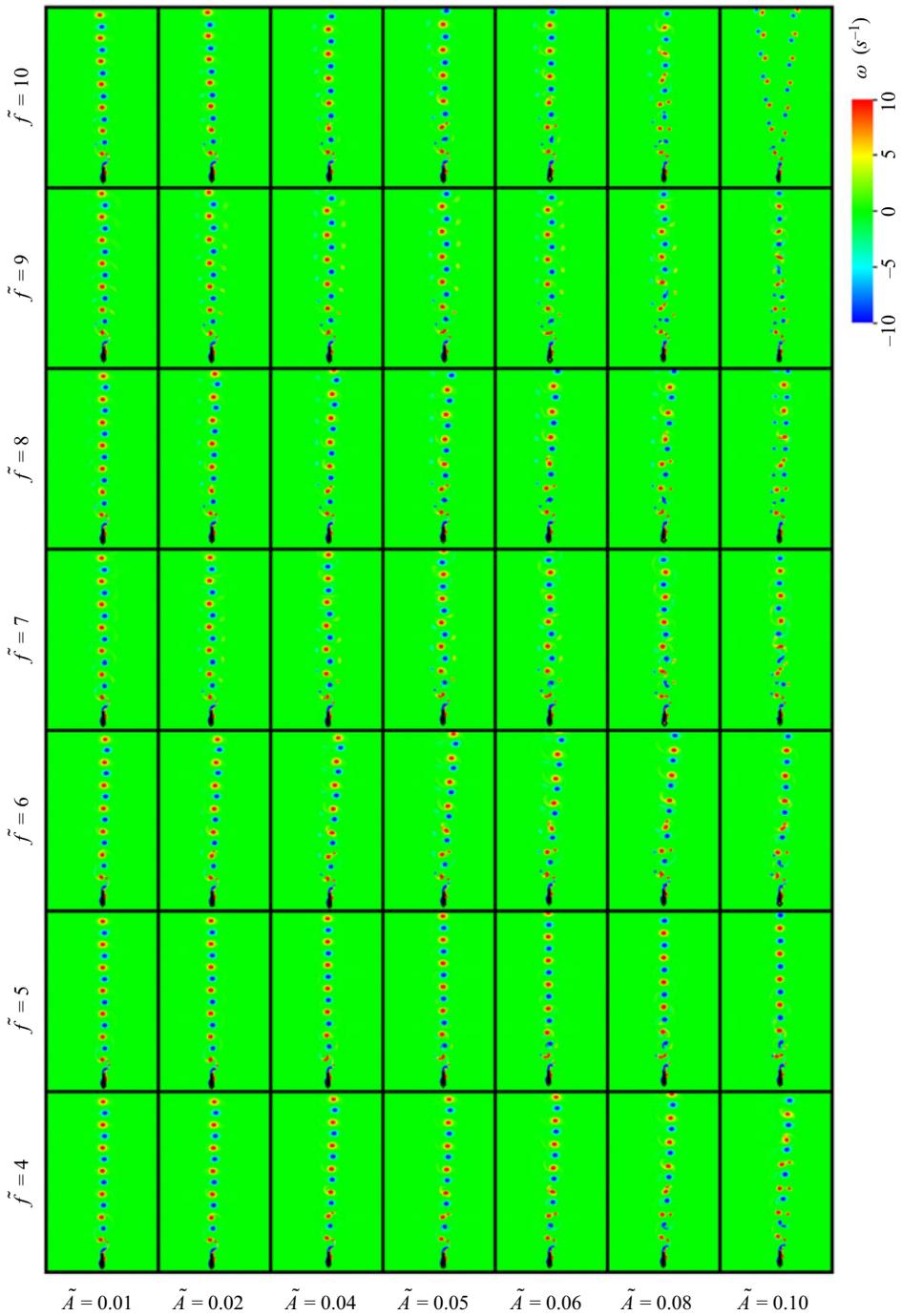
See figures 12 and 13.

Figure 12. Wake structures generated by the self-propelled pitching foil with perturbations.
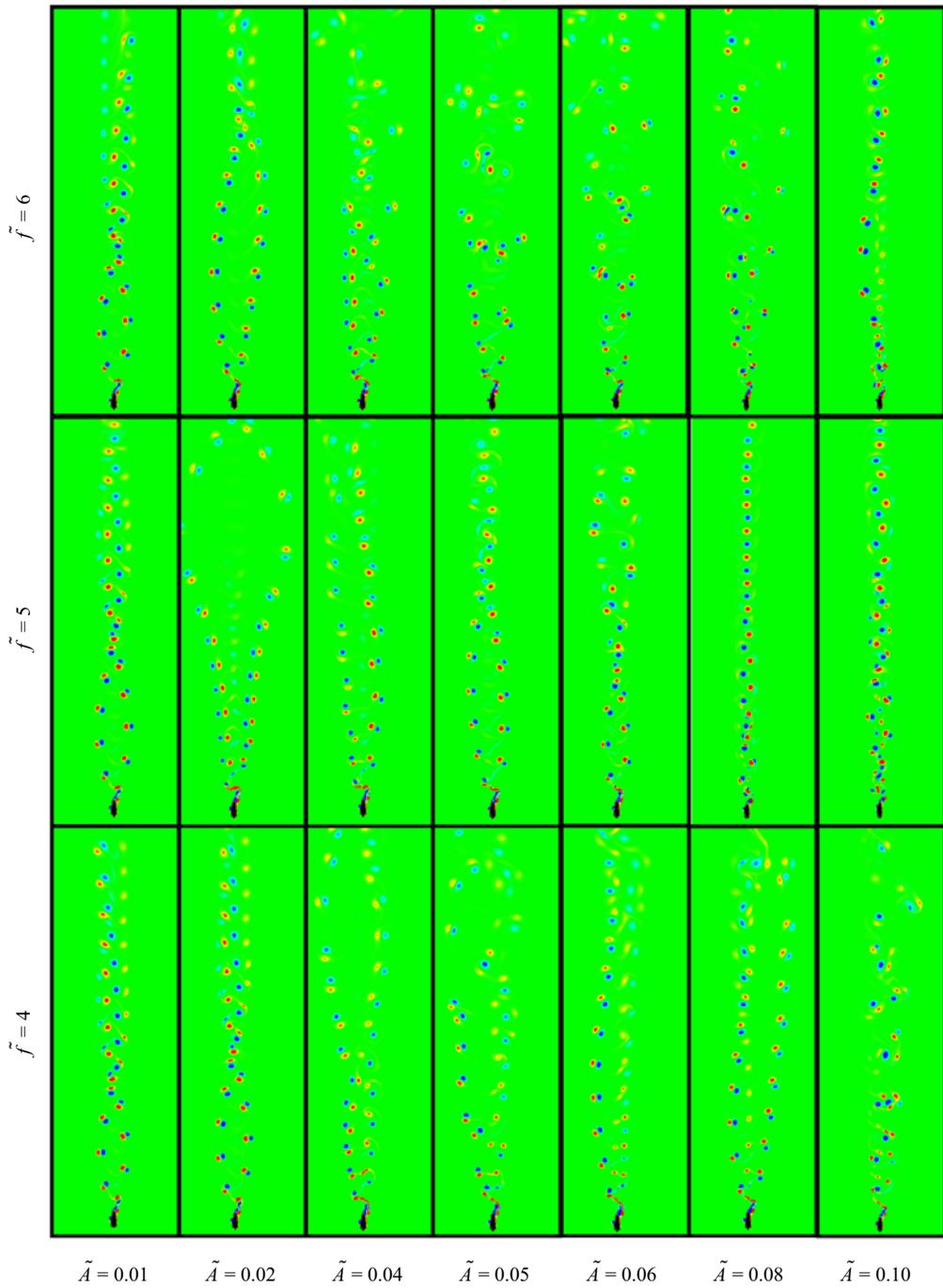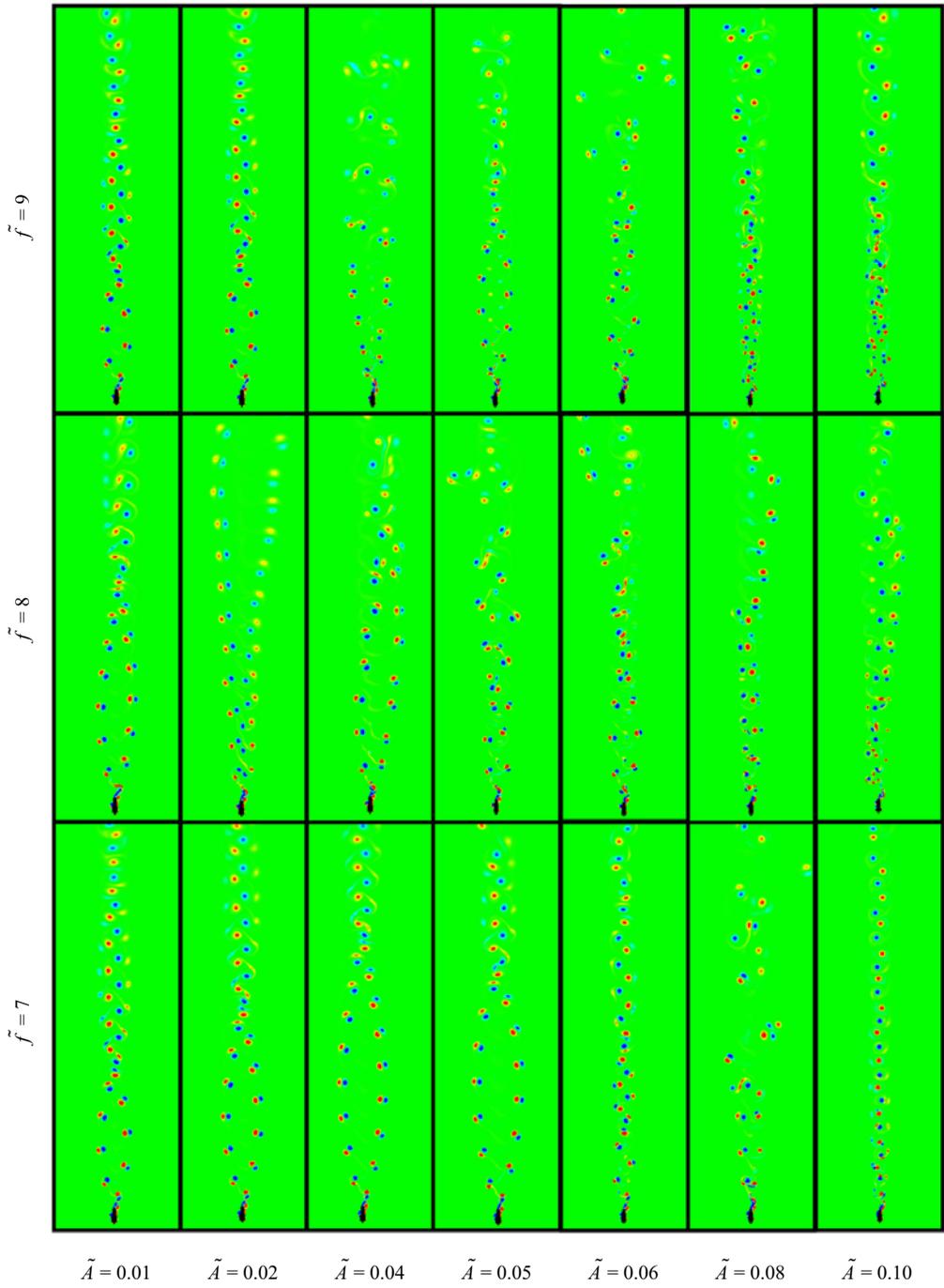
Figure 13. For caption see next page.

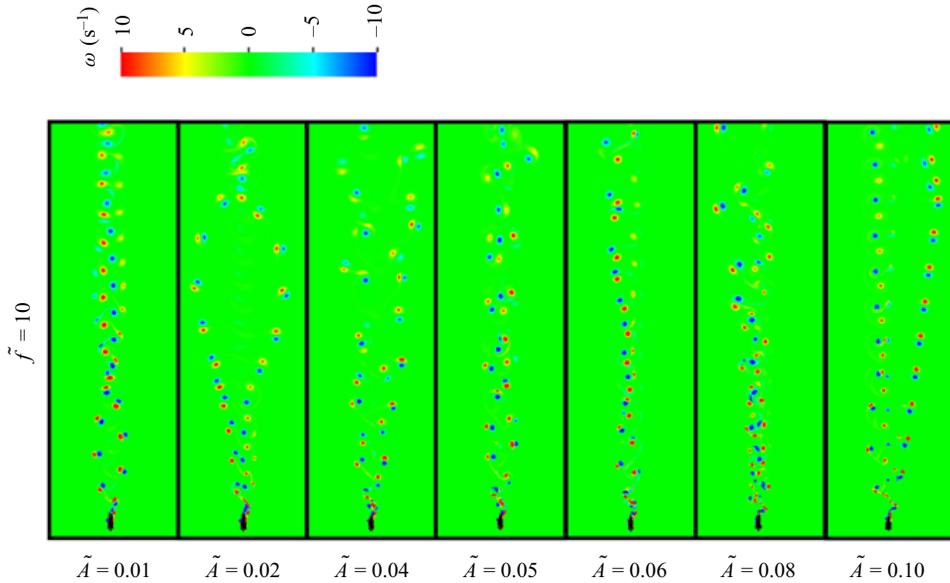Figure 13 (cntd). For caption see next page.

Figure 13 (cntd). Wake structures generated by the self-propelled heaving foil with perturbations.

Appendix C. Self-propelled pitching + heaving motion

We further simulated the swimming performance of the self-propelled foil undergoing the combined pitching and heaving motion (figure 14a). The kinematics of the BM is defined as

$$\left.\begin{aligned} \theta_b(t) &= \theta_{b\_max}\sin(2\pi f_b t + \psi), & \text{Pitching motion,} \\ h_{(t)} &= h_{b\_max}\sin(2\pi f_b t), & \text{Heaving motion,} \end{aligned}\right\} \tag{C1}$$

where ψ is the phase angle by which pitching motion leads to heaving motion. For BM, we considered $\sin(\theta_{b\_max}) = 0.15/0.9$, $h_{b\_max}/L = 0.15$, $\psi = 0$ and $f_b = 1$ Hz.

Since the perturbations can be superimposed into pitching motion:

$$\left.\begin{aligned} \theta_b(t) &= \theta_{b\_max}\sin(2\pi f_b t) + \theta_{p\_max}\sin(2\pi f_p t), & \text{Pitching motion with perturbations,} \\ h_{(t)} &= h_{b\_max}\sin(2\pi f_b t), & \text{Heaving motion,} \end{aligned}\right\} \tag{C2}$$

heaving motion:

$$\left.\begin{aligned} \theta_b(t) &= \theta_{b\_max}\sin(2\pi f_b t), & \text{Pitching motion,} \\ h_{(t)} &= h_{b\_max}\sin(2\pi f_b t) + h_{p\_max}\sin(2\pi f_p t), & \text{Heaving motion with perturbations,} \end{aligned}\right\} \tag{C3}$$

or both pitching and heaving motion:

$$\left.\begin{aligned} \theta_b(t) &= \theta_{b\_max}\sin(2\pi f_b t) + \theta_{p\_max}\sin(2\pi f_p t), & \text{Pitching motion with perturbations,} \\ h_{(t)} &= h_{b\_max}\sin(2\pi f_b t) + h_{p\_max}\sin(2\pi f_p t), & \text{Heaving motion with perturbations,} \end{aligned}\right\} \tag{C4}$$

984 A46-23
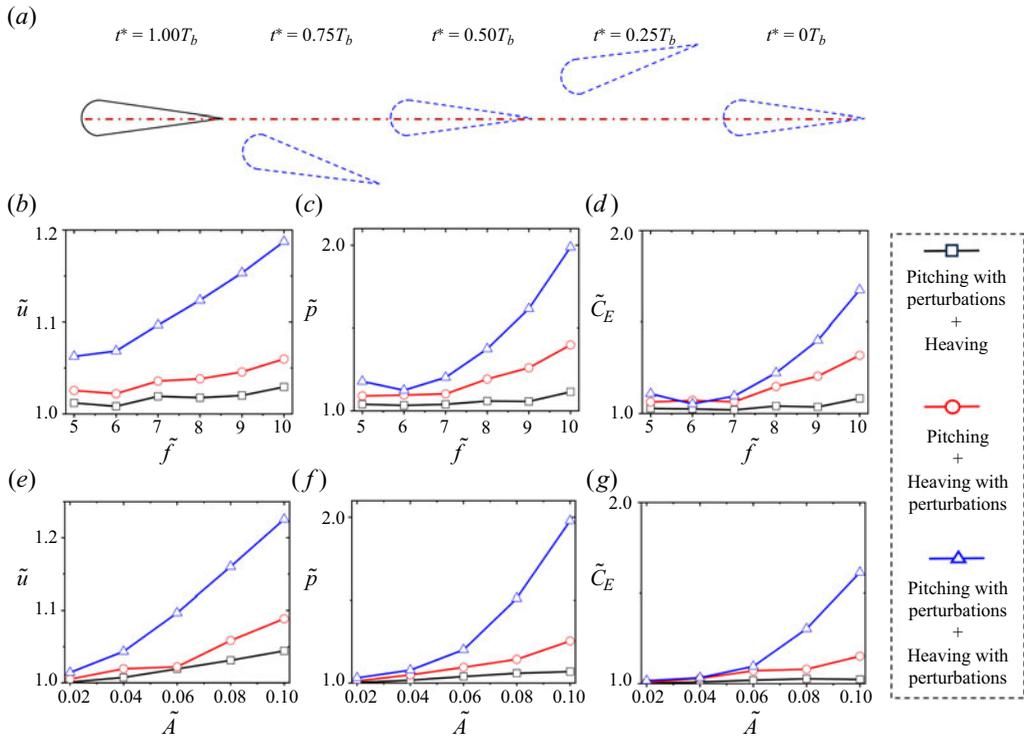
Figure 14. (*a*) Trajectory of pitching + heaving motion; dependence of (*b*) $\tilde{u}$, (*c*) $\tilde{P}$ and (*d*) $\tilde{C}_E$ on $\tilde{f}$ at $\tilde{A} = 0.06$; dependence of (*e*) $\tilde{u}$, (*f*) $\tilde{P}$ and (*g*) $\tilde{C}_E$ on $\tilde{A}$ at $\tilde{f} = 7$.

three scenarios, including pitching with perturbations + heaving motion, pitching + heaving with perturbations motion, and pitching with perturbations + heaving with perturbations motion, are considered. In each scenario, we considered $\tilde{A} = 0.06$ and varied $\tilde{f} = 5 - 10$ with an interval of $\Delta \tilde{f} = 1$ to study how different perturbations frequencies affect the swimming performance, and we fixed $\tilde{f} = 7$ and varied $\tilde{A} = 0.02 - 0.10$ with an interval of $\Delta \tilde{A} = 0.02$ to study the effects of perturbations amplitude.

As shown in figure 14(*b–d*), $\tilde{u}$ increases with an increase in $\tilde{f}$, while $\tilde{P}$ and $\tilde{C}_E$ first increase and then decrease when $\tilde{f}$ increases, with the minimal $\tilde{P}$ and $\tilde{C}_E$ obtained at $\tilde{f} = 6$. Figure 14(*e–g*) reveals that $\tilde{u}$, $\tilde{P}$ and $\tilde{C}_E$ increase with an increase in $\tilde{A}$. Particularly, figure 14(*b–g*) suggests that the kinematics combined pitching motion with perturbations and heaving motion with perturbations consume larger power and generate faster swimming speed, while the kinematics combined pitching motion with perturbations and heaving motion consume less power and generate slower swimming speed compared with other scenarios. Although we have not found energy saving in the present cases, we cannot reject the hypothesis that the self-propelled pitching + heaving motion would improve both swimming speed and efficiency generation since the interactions between pitching + heaving motion and relative perturbations are complicated. In future work, we will consider more conditions, such as refining the effect of the perturbation in the $\tilde{f} - \tilde{A}$ domain, superimposing the same/different perturbations into the pitching and heaving motion, and studying the effects of ψ values (or the maximal angle of attack).

984 A46-24

REFERENCES

ALAM, M.M. & MUHAMMAD, Z. 2020 Dynamics of flow around a pitching hydrofoil. *J. Fluids Struct.* **99**, 103151.

ANDERSEN, A., BOHR, T., SCHNIPPER, T. & WALTHER, J.H. 2017 Wake structure and thrust generation of a flapping foil in two-dimensional flow. *J. Fluid Mech.* **812**, R4.

BALE, R., HAO, M., BHALLA, A.P.S. & PATANKAR, N.A. 2014 Energy efficiency and allometry of movement of swimming and flying animals. *Proc. Natl Acad. Sci. USA* **111**, 7517–7521.

BECKER, A.D., MASOUD, H., NEWBOLT, J.W., SHELLEY, M. & RISTROPH, L. 2015 Hydrodynamic schooling of flapping swimmers. *Nat. Commun.* **6**, 8514.

BHALLA, A.P.S., BALE, R., GRIFFITH, B.E. & PATANKAR, N.A. 2013*a* A unified mathematical framework and an adaptive numerical method for fluid-structure interaction with rigid, deforming, and elastic bodies. *J. Comput. Phys.* **250**, 446–476.

BHALLA, A.P.S., GRIFFITH, B.E. & PATANKAR, N.A. 2013*b* A forced damped oscillation framework for undulatory swimming provides new insights into how propulsion arises in active and passive swimming. *PLoS Comput Biol.* **9**, e1003097.

BOMPHREY, R.J., NAKATAI, T., PHILLIPS, N. & WALKER, S.M. 2017 Smart wing rotation and trailing-edge vortices enable high frequency mosquito flight. *Nature* **544** (7648), 92–95.

CARLING, J., WILLIAMS, T.L. & BOWTELL, G. 1998 Self-propelled anguilliform swimming: simultaneous solution of the two-dimensional Navier–Stokes equations and Newton's laws of motion. *J. Exp. Biol.* **201**, 3143–3166.

CHAO, L.-M., ALAM, M.M. & JI, C. 2021 Drag–thrust transition and wake structures of a pitching foil undergoing asymmetric oscillation. *J. Fluids Struct.* **103**, 103289.

CHAO, L.-M., BHALLA, A.P.S. & LI, L. 2023 Vortex interactions of two burst-and-coast swimmers in a side-by-side arrangement. *Theor. Comput. Fluid Dyn.* **37**, 505–517.

CHAO, L.-M., JIA, L., WANG, S., LIBERZON, A., RAVI, S., COUZIN, I.D. & LI, L. 2024 Tailbeat perturbations improve swimming efficiency by reducing the phase lag between body motion and the resulting fluid response. *PNAS Nexus* **3**, pgae073.

CLEAVER, D. 2011 Low reynolds number flow control through small-amplitude high-frequency motion. PhD thesis, University of Bath.

CLEAVER, D., WANG, Z., GURSUL, I. & VISBAL, M.R. 2011 Lift enhancement by means of small-amplitude airfoil oscillations at low Reynolds numbers. *AIAA J.* **49** (9), 2018–2033.

FISH, F.E. & LAUDER, G.V. 2006 Passive and active flow control by swimming fishes and mammals. *Annu. Rev. Fluid Mech.* **38**, 193–224.

FLORYAN, D., VAN BUREN, T. & SMITS, A.J. 2018 Efficient cruising for swimming and flying animals is dictated by fluid drag. *Proc. Natl Acad. Sci. USA* **115**, 8116–8118.

FLORYAN, D., VAN BUREN, T. & SMITS, A.J. 2020 Swimmers' wake structures are not reliable indicators of swimming performance. *Bioinspir. Biomim.* **15** (2), 024001.

GAO, P., HUANG, Q. & PAN, G. 2021 Propulsion performance and wake dynamics of heaving foils under different waveform input perturbations. *J. Mar. Sci. Engng* **9**, 1271.

GARRICK, I.E. 1936 Propulsion of a flapping and oscillating airfoil. *NACA Tech. Rep.* 567. Neighborhood Assistance Corporation of America.

GAZZOLA, M., ARGENTINA, M. & MAHADEVAN, L. 2014 Scaling macroscopic aquatic locomotion. *Nat. Phys.* **10**, 758–761.

GODOY-DIANA, R., AIDER, J. & WESFREID, J.E. 2008 Transitions in the wake of a flapping foil. *Phys. Rev. E* **77** (1), 016308.

GRANGER, S. & PAÏDOUSSIS, M.P. 1996 An improvement to the quasi-steady model with application to cross-flow-induced vibration of tube arrays. *J. Fluid Mech.* **320**, 163–184.

GRIFFITH, B.E. & PATANKAR, N.A. 2020 Immersed methods for fluid–structure interaction. *Annu. Rev. Fluid Mech.* **52**, 421–448.

HAN, P., HUANG, W.-X., QIN, D., WANG, J. & ZHAO, J. 2023 An analytical model for estimating the maximum energy harvesting efficiency from vortex-induced vibration. *J. Fluids Struct.* **122**, 103961.

HOOVER, A.P., CORTEZ, R., TYTELL, E.D. & FAUCI, L.J. 2018 Swimming performance, resonance and shape evolution in heaving flexible panels. *J. Fluid Mech.* **847**, 386–416.

IBAMR 2014 IBAMR: An adaptive and distributed-memory parallel implementation of the immersed boundary method. Available at: https://ibamr.github.io/.

LAUDER, G.V., ANDERSON, E.J., TANGORRA, J. & MADDEN, P.G.A. 2007 Fish biorobotics: kinematics and hydrodynamics of self-propulsion. *J. Exp. Biol.* **210**, 2767–2780.

LEHN, A.M., THORNYCROFT, P.J.M., LAUDER, G.V. & LEFTWICH, M.C. 2017 Effect of input perturbation on the performance and wake dynamics of aquatic propulsion in heaving flexible foils. *Phys. Rev. Fluids* **2**, 023101.

MACKOWSKI, A.M. & WILLIAMSON, C.H.K. 2015 Direct measurement of thrust and efficiency of an airfoil undergoing pure pitching. *J. Fluid Mech.* **765**, 524–543.

MARQUET, L.B., RAMOSAND, O., BERGMANN, M. & IOLLO, A. 2021 Fluid–solid floquet stability analysis of self-propelled heaving foils. *J. Fluid Mech.* **910**, A28.

MITTAL, R. & IACCARINO, G. 2005 Immersed boundary methods. *Annu. Rev. Fluid Mech.* **37**, 239–261.

MULLER, U.K. & VAN LEEUWEN, J.L. 2004 Swimming of larval zebrafish: ontogeny of body waves and implications for locomotory development. *J. Exp. Biol.* **207** (5), 853–868.

PESKIN, C.S. 2002 The immersed boundary method. *Acta Numerica* **11**, 479–517.

QUINN, D.B., LAUDER, G.V. & SMITS, A.J. 2014 Scaling the propulsive performance of heaving flexible panels. *J. Fluid Mech.* **738**, 250–267.

TAYLOR, G.K., NUDDS, R.L. & THOMAS, A.L.R. 2003 Flying and swimming animals cruise at a Strouhal number tuned for high power efficiency. *Nature* **425**, 707–711.

TRIANTAFYLLOU, M.S., TRIANTAFYLLOU, G.S. & YUE, D.K.P. 2000 Hydrodynamics of fishlike swimming. *Annu. Rev. Fluid Mech.* **32**, 33–53.

TYTELL, E.D., LEFTWICH, M.C., HSU, C.-Y., GRIFFITH, B.E., COHEN, A.H., SMITS, A.J., HAMLET, C. & FAUCI, L.J. 2016 Role of body stiffness in undulatory swimming: insights from robotic and computational models. *Phys. Rev. Fluids* **1**, 073202.

WANG, S.Z., HE, G.W. & ZHANG, X. 2016 Self-propulsion of flapping bodies in viscous fluids: recent advances and perspectives. *Acta Mechanica Sin.* **32**, 980–990.

WILLIAMSON, C.H.K. & GOVARDHAN, R. 2004 Vortex-induced vibrations. *Annu. Rev. Fluid Mech.* **36**, 413–455.

WILLIAMSON, C.H.K. & ROSHKO, A. 1988 Vortex formation in the wake of an oscillating cylinder. *J. Fluid Struct.* **2**, 355–381.

YANG, D. & WU, J. 2022 Hydrodynamic interaction of two self-propelled fish swimming in a tandem arrangement. *Fluids* **7** (6), 208.

ZHANG, D., PAN, G., CHAO, L.-M. & ZHANG, Y. 2018 Effects of Reynolds number and thickness on an undulatory self-propelled foil. *Phys. Fluids* **30**, 071902.

ZHANG, D., ZHANG, J.-D. & HUANG, W.-X. 2022 Physical models and vortex dynamics of swimming and flying: a review. *Acta Mech.* **233**, 1249–1288.

ZHANG, J. 2017 Footprints of a flapping wing. *J. Fluid Mech.* **818**, 1–4.

ZHANG, X., NI, S.Z., WANG, S.Z. & HE, G.W. 2009 Effects of geometric shape on the hydrodynamics of a self-propelled flapping foil. *Phys. Fluids* **21**, 103302.

ZHU, X.J., HE, G.W. & ZHANG, X. 2014 How flexibility affects the wake symmetry properties of a self-propelled plunging foil. *J. Fluid Mech.* **751**, 164–183.